CHALMERS
UNIVERSITY OF TECHNOLOGY

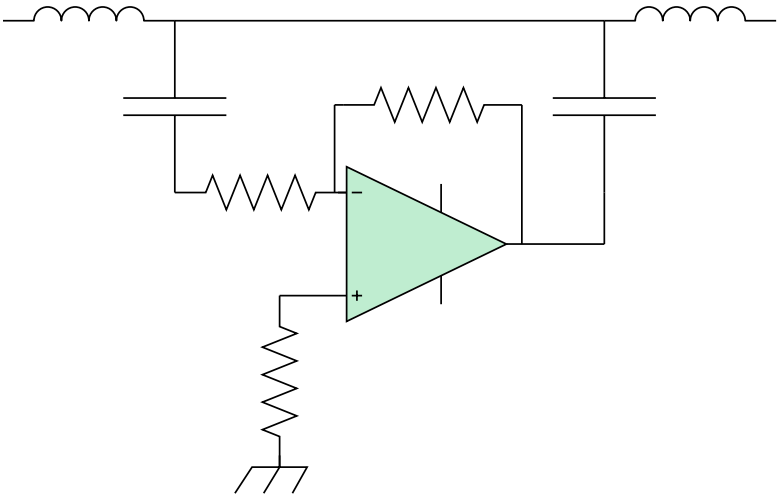

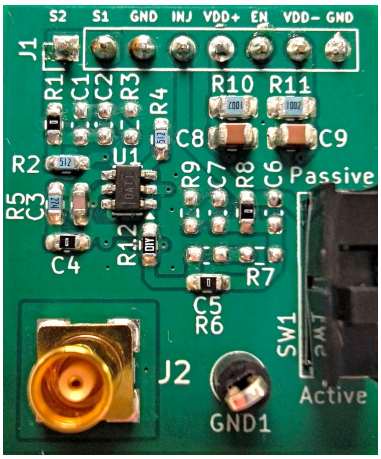

Design, Simulation and Implementation of an Active Common Mode EMI Filter for a DC/DC Application

Evaluation of a voltage sensing current injection type active EMI filter by replacing Y-capacitance in an existing passive filter

Master's thesis in Sustainable Electric Power Engineering and Electromobility

Edvin Karlsson
Edvin Nilsson

DEPARTMENT OF ELECTRICAL ENGINEERING

CHALMERS UNIVERSITY OF TECHNOLOGY
Gothenburg, Sweden 2026
www.chalmers.se

Master's thesis 2026

Design, Simulation and Implementation of an Active Common Mode EMI Filter for a DC/DC Application

Evaluation of a voltage sensing current injection type active EMI filter by replacing Y-capacitance in an existing passive filter

EDVIN KARLSSON
EDVIN NILSSON

CHALMERS
UNIVERSITY OF TECHNOLOGY

Department of Electrical Engineering
Division of Electric Power Engineering
Chalmers University of Technology
Gothenburg, Sweden 2026

Design, Simulation and Implementation of an Active Common Mode EMI Filter for a DC/DC Application
Evaluation of a voltage sensing current injection type active EMI filter by replacing Y-capacitance in an existing passive filter
EDVIN KARLSSON, EDVIN NILSSON

Supervisor: Dimitrios Meintanis. Aros Electronics, VANDEWIELE SWEDEN AB
Examiner: Torbjörn Thiringer - Chalmers University of Technology: Department of Electrical Engineering

Master's Thesis 2026
Department of Electrical Engineering
Division of Electric Power Engineering
Chalmers University of Technology
SE-412 96 Gothenburg
Telephone +46 31 772 1000

Cover: Simplified circuit of an active EMI filter and the produced prototype PCB.

Typeset in LaTeX
Printed by Chalmers Reproservice
Gothenburg, Sweden 2026

Design, Simulation and Implementation of an Active Common Mode EMI Filter for a DC/DC Application
Evaluation of a voltage sensing current injection type active EMI filter by replacing Y-capacitance in an existing passive filter
EDVIN KARLSSON, EDVIN NILSSON
Department of Electrical Engineering
Chalmers University of Technology

Abstract

This thesis implements an active common mode EMI filter in a DC/DC converter. Different topologies and strategies were analyzed and a voltage sense current injection type active filter was designed. The stability and performance were analyzed with analytical models, simulations and physical measurements. A stable active EMI filter was designed on a prototype PCB and was proven to attenuate common mode noise with up to 18 dB µV up to 700 kHz at 20 kW converter load. The inductance of the common mode chokes was then reduced, and it was verified theoretically and with low voltage measurements. An active filter with common mode chokes with 64 % lower inductance has a similar performance to a passive filter. This could however not be confirmed with 20 kW tests due to voltage limitations in the Op-amp of the active filter. An off the shelf IC from Texas Instruments was also evaluated, with good low voltage performance but saturated for high noise voltages when the converter was loaded with 20 kW.

Keywords: Active EMI Filter, AEF, VSCI, VSCC, CM, Common Mode, Hybrid EMI Filter

Acknowledgments

We want to thank our supervisor, Dimitrios Meintanis, for his guidance and support during our thesis project. His insights and encouragement have pushed our boundaries and strengthened our work as a whole.

We would also like to thank our examiner, Torbjörn Thiringer, for his constructive feedback throughout this project. We are thankful for his dedication and time.

We would also like to express our gratitude to Urban Lundgren for all his time and guidance with our measurements. His ideas during planning and support of measurements were essential to finishing the project.

Lastly, we would like to thank all employees at Aros Electronics for welcoming us and believing in us. Their positive support and encouragement from day one have not only made this thesis better but also made us enjoy this project so much more.

Thank You!

- Edvin Karlsson & Edvin Nilsson, Gothenburg, May 2026

List of Acronyms

Below is the list of acronyms that have been used throughout this thesis, listed in alphabetical order:

AC	Alternating Current
AEF	Active EMI Filter
BOM	Bill of Materials
CM	Common Mode
CMC	Common Mode Choke
CSCI	Current Sense Current Injection
CSVI	Current Sense Voltage Injection
DC	Direct Current
DM	Differential Mode
DMC	Differential Mode Choke
EMC	Electromagnetic Compatibility
EMI	Electromagnetic Interference
ESL	Equivalent Series Inductance
ESR	Equivalent Series Resistance
EUT	Equipment Under Test
EVM	Evaluation Module
FPGA	Field-Programmable Gate Array
GBP	Gain Bandwidth Product
GND	Ground
IC	Integrated Circuit
IL	Insertion Loss
LISN	Line Impedance Stabilization Network
MCX	Micro Coaxial Connector
Op-amp	Operational Amplifier
PCB	Printed Circuit Board
PE	Protective Earth
SPDT	Single Pole Double Throw
TI	Texas Instruments
TVS	Transient Voltage Suppressor
UN ECE	United Nations Economic Commission for Europe
VNA	Vector Network Analyzer
VSCC	Voltage Sense Current Compensation
VSCI	Voltage Sense Current Injection
VSVI	Voltage Sense Voltage Injection

Contents

1
Introduction

With the increasing demand for power density in power electronics equipment, a higher switching frequency is often required. The higher frequency demands a deep understanding of Electromagnetic Compatibility (EMC), as higher switching frequencies generate more Electromagnetic Interference (EMI) [1]. It is therefore important to analyze and reduce the product's EMI to limit compatibility issues between devices and pass legal requirements for specific applications. EMI reduction is achieved by filtering, commonly by passive filters, but more recently also with active filters [2]. Active EMI Filters (AEF) are a promising technique for improving the performance and reducing the physical size of EMI filters [3], [4], [5]. This thesis investigates the possibility of implementing an active filter in a DC/DC application. The DC/DC converter is operating at 700 V, 20 kW with a switching frequency of 100 kHz.

This chapter introduces the background to EMI filters and Active EMI filters together with the aim and limitations of this report.

1.1 Background

Conducted EMI is split into Common Mode (CM) noise and Differential Mode (DM) noise. The former is typically more challenging to mitigate than DM due to the limitations in Y-capacitance. The total Y-capacitance is typically limited for safety reasons, as high currents can lead to high voltages in the chassis [6]. Hence, to get attenuation at lower frequencies, Common Mode Chokes (CMCs) can be used. But they tend to be very large, occupying a significant volume of the product. Therefore, there is a need for an alternative to traditional passive filters in order to allow for converters with a smaller size and volume.

Active EMI filtering uses an active circuit to mitigate the noise by measuring the EMI noise and injecting an opposing cancellation signal. There have been numerous research studies on the theory and analysis of AEFs, many of which suggest AEFs work effectively over a wide range of frequencies [7], [8]. One common issue is the AEF stability [1]. Multiple solutions to this problem have been proposed in the literature, but there is a lack of practical implementations with experimental verification. There are also a limited number of commercially available AEFs on the market. One that has gotten attention in the literature is the integrated circuit (IC) from Texas Instruments (TI) [9].

As there is an insufficient number of practical implementations of AEFs, more research is needed. This report aims to further close that gap. This is done through analytical calculations, simulations and experimental work.

1.2 Aim

This study aims to analyze the function and performance of an active EMI filter and implement a proposed design. Measurements are to be performed to understand and evaluate the practical challenges and opportunities of active EMI filtering for a bidirectional DC/DC converter.

The study also aims to investigate how optimal performance is achieved, in terms of stability, network design and amplifier selection. The performance of a traditional passive filter, a purchased off the shelf AEF and a proposed AEF circuit will be compared and analyzed. The research questions can be summarized as:

- How much can an active EMI filter reduce the CM noise?
- How does a purpose built AEF with discrete components perform compared to a passive filter and an off the shelf IC?
- How much can the CMC size be reduced together with active filters and still perform similarly to passive filters?

1.3 Limitations

This report is limited to the analysis and development of a CM AEF for conducted emissions; DM and radiated EMI will not be considered.

Even if the overall benefit of an active filter is to reduce the size of the passive components in a passive filter, a smaller size passive filter will not be built. Instead, the inductance in the CMCs will be reduced by removing turns in the CMCs and the resulting smaller size will be calculated from the reduced inductance.

The voltage supply of the Op-amps will not be covered in this study, as it requires converting the DC/DC converter's operating voltage of 700 V to $\pm$ 5 V in a safe and stable way that does not affect EMI emissions.

The active filter will be limited to a completely analog design.

2
Theory

In this section, previously known theory relevant to the subject are presented. The definitions of EMI and the theory of passive and active filtering will be presented, along with the instruments and software used.

2.1 Differential- and Common Mode EMI

EMI consists of radiated and conducted EMI, where the conducted EMI is typically regulated within the range of 150 kHz to 30 MHz in standards [10]. Radiated emissions are however transmitted as electromagnetic waves, typically regulated in the frequency range of 30 MHz to 1 GHz [10].

Conducted EMI can be further classified into DM and CM EMI noise, where DM noise is where the current has the opposite direction and CM noise is where the current has the same direction [11]. DM and CM noise propagation paths are illustrated in Figure 2.1.

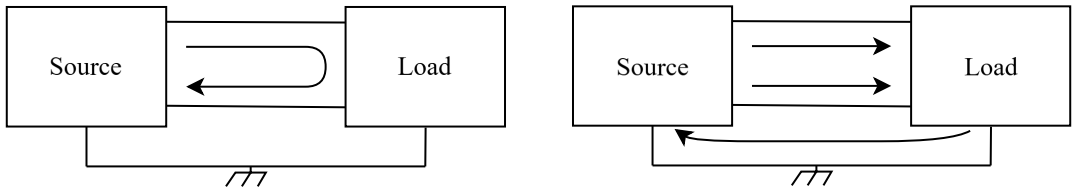

(a) Differential mode noise path. **(b)** Common mode noise path.

Figure 2.1: Common mode and differential mode propagation paths.

The DM path illustrated in Figure 2.1a shows the current flowing from the positive back to the negative conductor, while the CM path illustrated in Figure 2.1b shows the current flowing in the positive and negative conductors back through the chassis ground.

Differential mode noise is typically caused by switching noise and oscillations, while CM noise is caused by currents to the chassis ground due to stray capacitance [11]. DM noise can be mitigated with capacitors between the positive and negative conductors (X-capacitors) and series inductors [2], [12]. CM noise can be reduced with capacitors between the positive or negative conductors and chassis ground (Y-capacitors) and CMCs, where inductors share a core for both positive and negative lines [2],[6].

2.2 Passive EMI Filter

A passive EMI filter usually consists of some configuration of at least one CMC and one Differential Mode Choke (DMC). The difference between the CMC and DMC is illustrated in Figure 2.2.

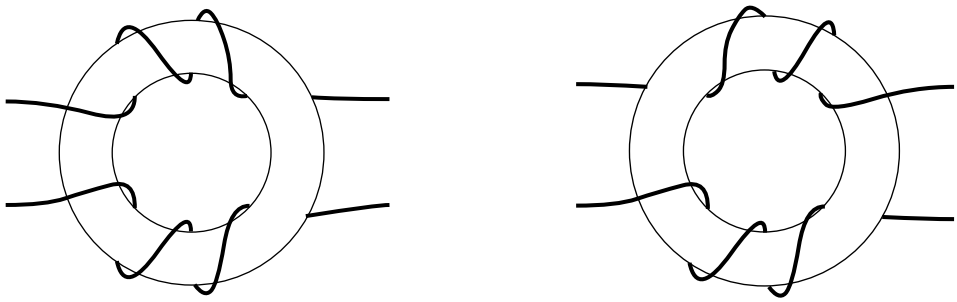

(a) Conductors wound symmetrically. **(b)** Conductors wound asymmetrically.

Figure 2.2: Winding arrangement of a Common Mode Choke (a) and a Differential Mode Choke (b). In these cases, three turns for each conductor.

The different types of chokes illustrated in Figure 2.2 are similar apart from the winding directions. Figure 2.2a shows a typical CMC, where the conductors are wound symmetrically, while Figure 2.2b shows a typical DMC, where the conductors are wound asymmetrically. For CM noise, the CMC winding configuration generates magnetic flux from both windings that add to each other, thereby increasing the impedance and damping the CM noise [13]. In a DMC, the DM noise currents in the windings generate magnetic flux that adds together and thus increases the impedance. This dampens the DM noise [12].

Often, capacitance connected between lines and chassis ground, called Y-capacitance, is also used to mitigate CM noise. Y-capacitance does this by leading away CM noise by creating a shorter low impedance path to ground [12]. This method, however, has its limits as a large Y-capacitance can create large earth leakage currents. This current must be limited for safety reasons as this current can harm people [6]. Therefore, Y-capacitance is limited in size. The limited Y-capacitance causes the CMCs to be large in size, as high inductance is required to obtain a sufficiently low cutoff frequency [13].

In the same way, by connecting capacitors directly between the two lines, DM noise is mitigated through this low impedance path [12].

2.3 Common Mode Representation

As many applications of a passive EMI filter consist of two conductors for current in addition to Protective Earth (PE), it is common to represent this as a CM equivalent circuit featuring only one conductor and PE [14]. Figure 2.3a presents the common three-wire circuit and Figure 2.3b represents its respective CM circuit representation.

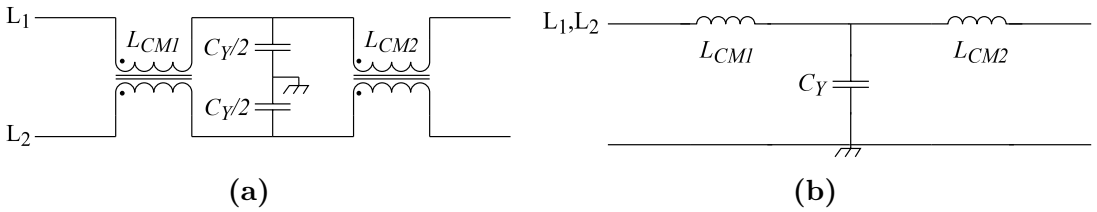

Figure 2.3: Common mode EMI filter represented as (a) Three line circuit (b) Equivalent common mode circuit.

The three wire circuit seen in Figure 2.3a can be reduced to the circuit seen in Figure 2.3b [14]. This representation is only valid for analyzing CM noise, as CM noise is conducted in both positive and negative conductors, which are therefore short circuited. The CM representation simplifies calculations and simulations regarding CM noise.

2.4 Usage of Line Impedance Stabilization Network

In order to measure the conducted EMI of the Equipment Under Test (EUT), which is the DC/DC converter with the EMI filter, a stable and standardized impedance on the power input is required. This is achieved by implementing a Line Impedance Stabilization Network (LISN) on the power input of the EUT [15]. The LISN also blocks external noise from reaching the EUT [16]. In addition, EMI emissions can be measured in the LISN port defined as U. The CISPR 25 standard, for automotive applications, defines the LISN according to Figure 2.4 [17].

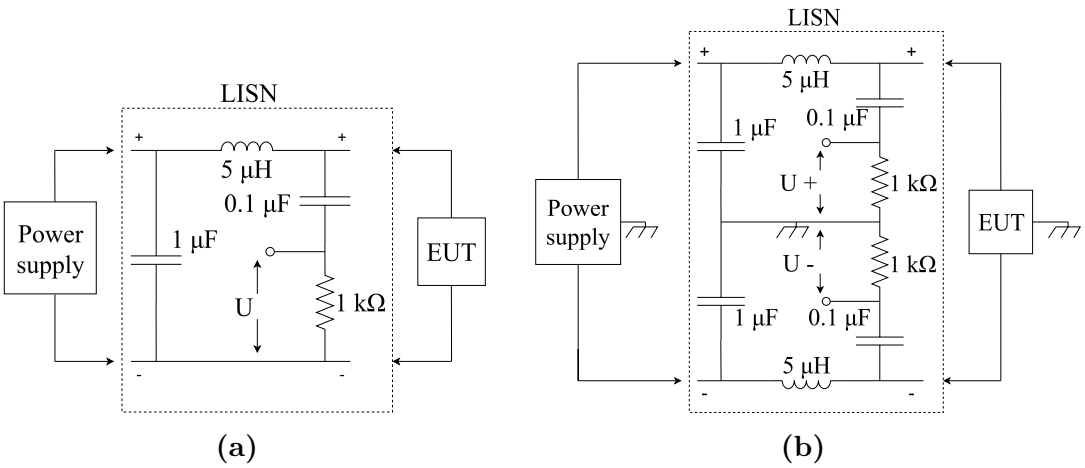

Figure 2.4: LISN defined by the CISPR 25 standard 2016. (a) Implementation in ground-negative applications using a single LISN. (b) Implementation in +/- and chassis ground connection utilizing two LISNs.

The LISN in Figure 2.4a is built for a two-conductor system. In the case of a product with a positive and negative conductor, as well as a protective ground or chassis

ground, the system in Figure 2.4b consisting of two LISN units in parallel shall be used [17]. In that case, the EMI is measured at both the positive and negative ports ($U+$ and $U-$), and both must be within the limits of the requirements. During the measurements, the HV-AN 150 LISN manufactured by Teseq was used [18].

2.5 Definition of Insertion Loss

In order to measure the performance of a filter, IL is often used [19]. It is defined as the noise current flowing through a LISN without a filter implemented, divided by the noise current measured through a LISN with a filter implemented [7]. This results in

$$IL = \frac{I'}{I} \tag{2.1}$$

where I' is the measured noise current without a filter and I is the noise current measured with a filter [7]. A low I compared to I' indicates a good filter where IL in (2.1) increases for better filters. IL is therefore a measure of filter attenuation performance [7].

When both input and output impedances are $50\,\Omega$, the IL can be measured by the scattering parameter S_{21} and IL can be calculated as

$$IL = \frac{1}{S_{21}} \tag{2.2}$$

or if S_{21} is measured in dB, it can be calculated as

$$IL(\text{dB}) = -S_{21}(\text{dB}) \tag{2.3}$$

as shown in [20].

2.6 Active EMI Filter

The first generalization of AEF topologies was presented in [21] and the Insertion Loss (IL) was derived in [22]. These analyses were extended and generalized in [23].

EMI filters consist of three distinct components; noise sensing, noise processing and noise canceling injection. The noise can be sensed through current with a high bandwidth current transformer [24],[25], or by sensing the voltage with a capacitive circuit [26], [27]. The processing is typically done with an analog amplifier, but digital solutions using an FPGA have also been presented in the literature with good results [28]. Noise canceling injection can be done by injecting a current with a capacitive circuit [24], [1], or by injecting a voltage with a voltage transformer [25], [29].

The general control scheme can be either a feedback circuit or a feedforward circuit. If a feedforward circuit is used, it is practically necessary to measure and inject the same quantity. Otherwise, very accurate mapping of the impedances of the system is

required, and small variations will have large effects on the performance. In addition, the two remaining feedforward structures require good mapping of the components, especially parasitics at higher frequencies [30], which makes them unfeasible for this application. The available topologies of feedback types are summarized in Figure 2.5.

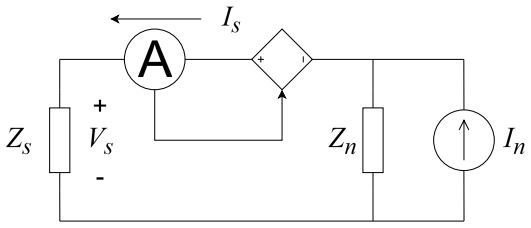

(a) Current Sense Voltage Injection (CSVI).

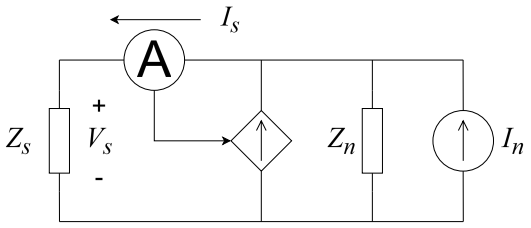

(b) Current Sense Current Injection (CSCI).

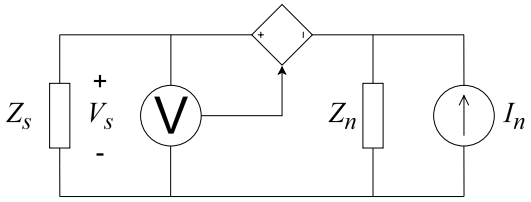

(c) Voltage Sense Voltage Injection (VSVI).

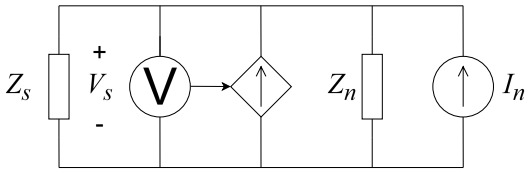

(d) Voltage Sense Current Injection (VSCI).

Figure 2.5: Simplified circuit models for (a) CSVI, (b) CSCI, (c) VSVI and (d) VSCI.

CSVI in Figure 2.5a measures the current and injects a voltage to mitigate the noise, CSCI in Figure 2.5b measures the current and injects a current. VSVI in Figure 2.5c senses the noise voltage and injects a voltage and VSCI in Figure 2.5d measures the voltage and injects a current.

For the given topologies, the insertion loss IL and the condition for maximum insertion loss can be expressed as in Table 2.1 [23], where A_i is the amplifier gain of the different topologies. A_1 and A_4 are pure gains, while A_2 is a trans-conductance [A/V] and A_3 is a trans-resistance [V/A]. Z_n is the load (noise source) impedance and Z_s is the power source (LISN) impedance. Y is the admittance which is the inverse of impedance.

Table 2.1: Insertion loss and condition for maximum IL for VSVI, VSCI, CSVI and CSCI AEF topologies.

Type	IL	Condition for maximum IL
VSVI	$1 + \frac{A_1 Zs}{Z_s + Z_n}$	$\|Z_s\| >> \|Z_n\|$
VSCI	$1 + \frac{A_2}{Y_s + Y_n}$	$\|A_2\| >> \|Y_s + Y_z\|$
CSVI	$1 + \frac{A_3}{Z_s + Z_n}$	$\|A_3\| >> \|Z_s + Z_n\|$
CSCI	$1 + \frac{A_4 Z_n}{Z_s + Z_n}$	$\|Z_n\| >> \|Z_s\|$

In Table 2.1, the criteria for high IL of VSVI type filters are that the source impedance should be much larger than the load impedance. This is valid for ideal voltage sources or capacitive loads. For CSVI type filters, the gain must be larger than the sum of the load and source impedances. In other words, this topology is good for loads with low impedance. VSCI type filters are effective when the gain is larger than the sum of the system's admittances, which occurs when the source and load impedances are large. CSCI type filters are effective when the load impedance is much larger than the source impedance, which is valid for ideal current sources and inductive loads.

In [4], these results are elaborated further, where it is noted that for CM noise, the load impedance is usually in the order of 10 kΩ to 100 kΩ, while the load impedance for DM noise is in the order of 10 Ω to 100 Ω Therefore, current injection type filters are more suitable for CM noise, while voltage injection methods are more suitable for DM noise. Article [4] also presents analytical and experimental results to support this claim.

2.7 DC Bias of Ceramic Capacitors

Due to the ceramic materials used in ceramic capacitors, the ceramic becomes polarized and anti-polarized when a DC voltage is applied and removed respectively. This effect in turn, changes the capacitance of ceramic capacitors [31]. A larger DC bias voltage results in a smaller capacitance value [31]. This effect must be considered when designing for applications where DC bias will be present [31].

2.8 Texas Instruments IC TPSF12C1

One of the few commercially available ICs designed solely for EMI noise canceling is the Texas Instruments TPSF12C1. This chip works on the VSCI principle. A stabilization filter, sensing capacitors and injection capacitors are not included in the chip [9]. These should be mounted outside the chip as these component values are adjustable [9]. There is an Evaluation Module (EVM) available named TPSF12C1QEVM featuring this Texas Instruments IC [32]. The evaluation board includes a stabilization filter, in which the component values are calculated using the

provided design calculation tool [33]. The EVM has 0603 footprints for the passive components, and the whole PCB measures 25 mm by 20 mm [32].

2.9 Software and Instruments Used

This section introduces and explains different instruments, software simulation tools and measurement tools used throughout this thesis.

2.9.1 LTspice

LTspice is a simulation software used to simulate electrical circuits. The software features a graphical interface with a waveform viewer to analyze circuits in detail [34]. This software is based on the open-source Simulation Program with Integrated Circuit Emphasis (SPICE) developed in 1973 at the University of California, Berkeley [35].

2.9.2 Omicron Bode 100 Vector Network Analyzer

The Bode-100 Vector Network Analyzer (VNA) is a multifunctional instrument that can be used for various measurements, such as impedance, gain and scattering parameter measurements [36]. It has one output with a signal generator and two measurement ports. It can be used to measure parasitics, loop gain or transmission parameters in a simple way.

The Bode-100 instrument is controlled by the bundled software, Bode Analyzer Suite, which enables graphical presentations of results and data exports [37]. The software also features Circuit Fit, which fits a circuit model to a measured impedance.

2.9.3 TEKBOX TBLM01 LISN MATE

A TEKBOX LISN MATE can be used to separate DM and CM emissions from a two LISNs measurement [38]. The box has two inputs, one from each LISN and two outputs, one for DM and one for CM. The output that is not connected to the EMI receiver should be terminated with 50 Ω to not affect the impedance. The CM and DM impedances are not perfectly 50 Ω as the box is not ideal, but the measurements can still provide insight into whether the emissions are DC or CM.

3

Development of Active EMI Filter

The following chapter presents the simulations and decisions made during the AEF's development phase. Later, the final prototype Printed Circuit Board (PCB) is presented.

3.1 Component Characterization for Modeling and Simulations

The CMCs are far from ideal components. They are big and have stray capacitance between windings, leakage inductance and skin effect among other parasitics. Because the characteristics of the CMCs affect the filter´s behavior and resonances, it is important to accurately characterize the CMCs in the simulation and modeling of the filter. This enables the tuning of filter parameters correctly. A Bode 100 instrument was used to characterize the CMC using its impedance measurement setting.

To represent the measurement of the CMCs in simulations, the impedance measurement was fitted to a RL-C-R model shown in Figure 3.1a and to a four pole R-L-C series network model. Figure 3.1b shows the R-L-C series network for two poles. The four pole R-L-C series network used is modeled with the same structure as in Figure 3.1b, but with four poles. This fitment was done with the internal Circuit Fit function in the Bode 100 software.

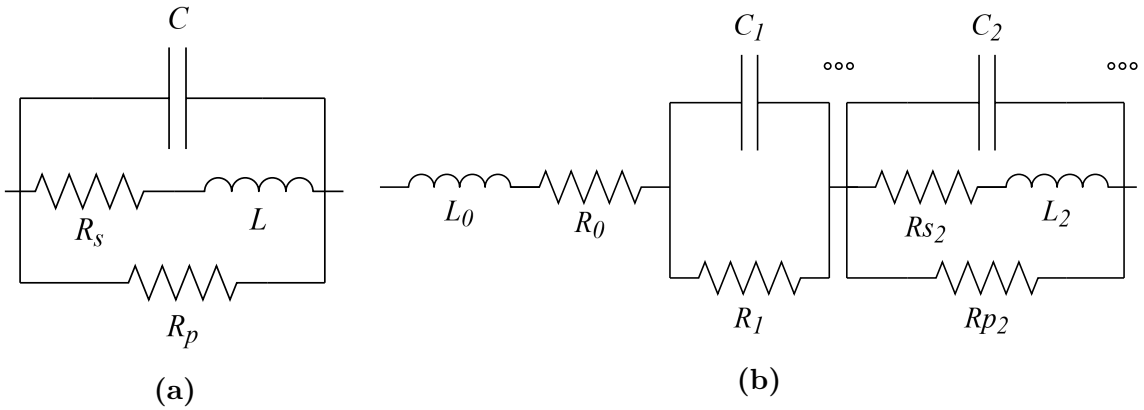

Figure 3.1: Circuit fit of CMC with (a) RL-C-R model and (b) R-L-C series network.

The simple representation shown in Figure 3.1a includes the common parasitics in an inductor. This includes; Parallel resistance R_p, Parallel capacitance C_p and Series resistance R_s. This model however, did not provide a good representation throughout the frequency range. Instead, the 4 pole R-L-C series network shown in Figure 3.1b was used as this representation provided a good fit throughout the frequency range.

The impedance of the CMC resulting from the Bode 100 measurement is presented in Figure 3.2.

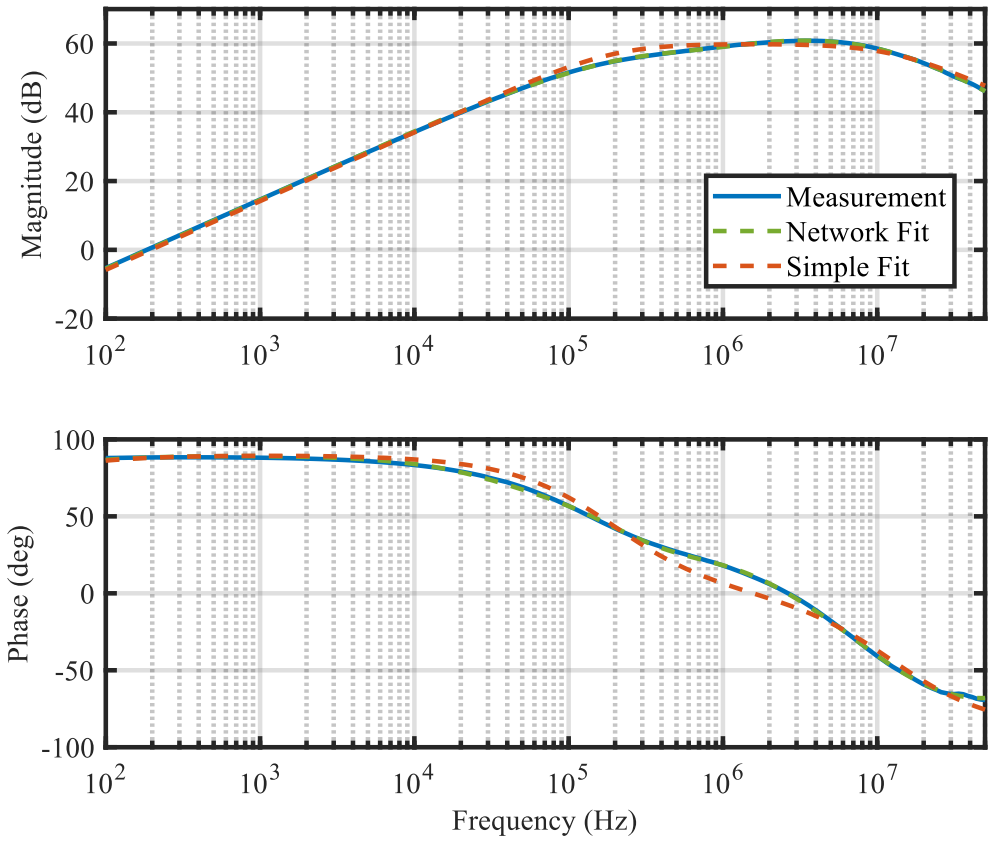

Figure 3.2: Measured and fitted Impedance of CMC, where Simple fit denotes the RL-C-R model and Network fit denotes the 4 pole R-L-C series network.

Figure 3.2 shows the two models compared to the actual impedance measurement. It is clear that the Network fit provides a better fit than the Simple fit across all measured frequencies. Because the network model performed well across all frequencies within the relevant range, it was used in all simulations. The fitted model was exported to LTspice as a SPICE model and as a vector into MATLAB and was used in the CM equivalent model.

Other components were modeled with their Equivalent series resistance (ESR) and Equivalent series inductance (ESL). ESR and ESL were measured with the Bode

100 instrument with an Omicron B-WIC impedance adapter which provides a four wire Kelvin connection.

3.2 Existing Passive Filter

The passive filter used in this project is the filter already implemented in the DC/DC converter. The schematic for the passive filter is presented in Figure 3.3. This filter was developed prior to this study.

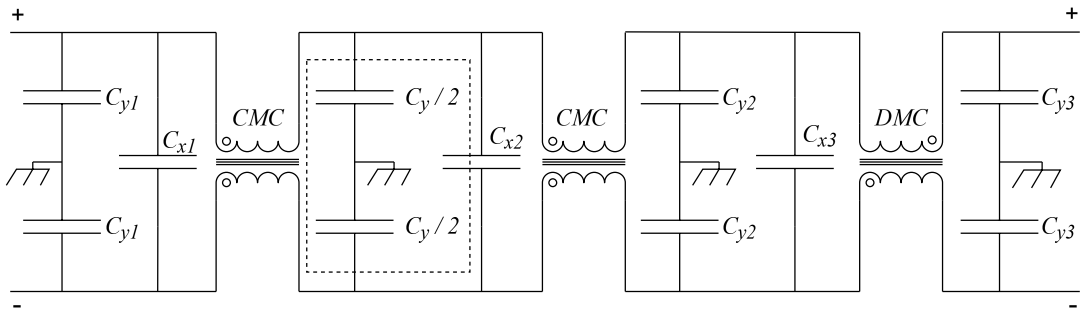

Figure 3.3: Schematic of the already implemented passive EMI filter in the DC/DC converter.

In Figure 3.3, the main components of the CM filter are the two CMCs with 5 turns each, and the two highlighted Y-capacitors $C_y/2$, which together make up the bulk of the Y-capacitance. In addition, there are smaller Y-capacitors C_{y1}, C_{y2} and C_{y3} with the main purpose of attenuating high frequency noise, as well as separating the different stages in the filter. All Y-capacitors in the passive filter are ceramic capacitors. The remaining components, which are the X-capacitors and the DMC are for DM filtering and will not be considered in this study.

In the DC/DC converter in which this filter was implemented, the Y-capacitance is limited due to safety reasons. Therefore, an AEF was implemented to replace only the two $C_y/2$ capacitances. The capacitance of C_y is 37.6 nF. Therefore, the sum of the sensing capacitors and the injection capacitors must not exceed this value.

3.3 Choice of Topology and Implementation into Existing Passive Filter

As described in the Theory section, the current injection topologies are most suitable for CM mitigation. This type of injection is also preferable because it does not require an additional transformer, unlike the voltage injection type. Therefore, because of performance and simplicity, this type of injection is chosen.

Current sensing generally provides better stability than voltage sensing, but voltage sensing is still preferred here, as it does not require an additional transformer or

modifications to the existing CMCs. The VSCI topology is therefore chosen, as it allows for a very small size without any transformers and still offers seemingly good performance.

The implementation into the existing passive filter is done by replacing both $C_y/2$ shown in Figure 3.3, with the active VSCI filter. Note that both sensing and injection are done in this node between the CMCs.

The main purpose of using an AEF is to reduce the size of the CMCs, and hence the size of the whole EMI filter. The reason why the CMCs are large in size is to obtain a low cutoff frequency to attenuate the low frequency EMI. Therefore, it is crucial that the AEF focus on the lower frequencies, as this allows for designing and optimizing the passive parts for higher frequencies, which generally results in lower component values and smaller physical size. In this specific study, the filter is applied to a DC/DC converter with 100 kHz switching frequency. If a perfect square wave is assumed, 300 kHz will be the most important frequency as this square wave contains all odd harmonics of the fundamental frequency, and 100 kHz is outside the measured EMI spectrum.

3.4 Modeling of AEF

Analytical expressions for IL for active and hybrid topologies have been derived in various literature. However, the authors have not found any expressions for the selected filter topology in this study. The IL is therefore derived below from the ABCD parameters by considering the filter as a four pole shown in Figure 3.4. The modeling is done with CM representation to simplify analysis. To further simplify the analytical models, only the basic structure of the filter was considered.

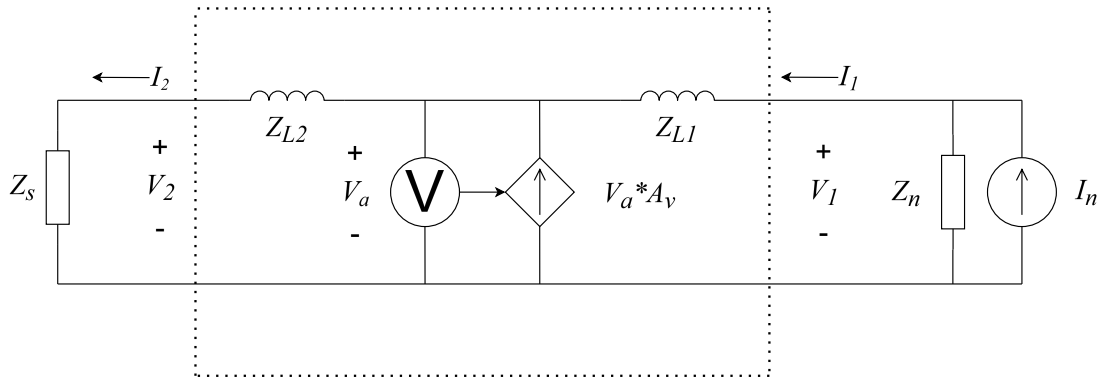

Figure 3.4: Four pole representation of a hybrid filter.

In Figure 3.4, Z_n represents the common mode impedance of the noise source, and Z_s is the common mode impedance of the source to the DC/DC converter. Z_{L1} and Z_{L2} are the impedances of the first and second CMC respectively. V_a is the measured voltage noise, A_v is the amplification coefficient, resulting in an injected current $I_{inj} = V_a A_v$. The input of the four pole has voltage V_1 and current I_1 and

the output V_2 and I_2.

The insertion loss IL from a four pole can be calculated as

$$IL = \frac{AZ_n + B + CZ_sZ_n + DZ_s}{Z_s + Z_n} \tag{3.1}$$

where A, B, C and D are the ABCD parameters. By using the definitions of the ABCD parameters and expressing them as

$$A = \frac{V_1}{V_2}\Big|_{I_2=0} = Z_{L1}\left(\frac{1}{Z_{L1}} + A_v\right) \tag{3.2a}$$

$$B = \frac{V_1}{I_2}\Big|_{V_2=0} = Z_{L1}\left(1 + \frac{Z_{L2}}{Z_{L1}} + Z_{L2}A_v\right) \tag{3.2b}$$

$$C = \frac{I_1}{V_2}\Big|_{I_2=0} = A_v \tag{3.2c}$$

$$D = \frac{I_1}{I_2}\Big|_{V_2=0} = 1 + A_vZ_{L2} \tag{3.2d}$$

, the insertion loss can be expressed as

$$IL = \frac{1}{Z_n + Z_s}\left(Z_n + Z_{L1} + Z_{L2} + Z_s + A_v\left(Z_nZ_{L1} + Z_{L1}Z_{L2} + Z_sZ_n + Z_sZ_{L2}\right)\right). \tag{3.3}$$

Note that when $Z_{L1} = 0$ and $Z_{L2} = 0$, the insertion loss becomes

$$IL = 1 + A_v\left(\frac{Z_sZ_n}{Z_s + Z_n}\right) \tag{3.4}$$

which yields the same result as the purely active filter [4]. It also means that a higher insertion loss is given if both the noise impedance and the source impedance are high, which is the case for CM emissions. It is also worth noting that if Z_s and Z_n are equal, Z_{L1} and Z_{L2} should also be equal for the best performance. Furthermore, it is important to keep in mind that the amplification A_v is not constant and will depend on frequency and impedance.

To determine the parameter A_v, the voltage controlled current source must be analyzed. A model for a pure active filter was presented in [7]. The model has been adjusted for the hybrid filter with CMCs. By defining the gain G_{hpf} as the transfer function of the high-pass filter of the sensing capacitor and G_{amp} as the transfer function of the amplifier, the injected current I_{inj} can be calculated as

$$I_{inj} = \frac{V_a - V_a\left(G_{hpf}G_{amp}\right)}{Z_{inj} + Z_{clo}} \tag{3.5}$$

where Z_{inj} is the impedance of the injection capacitor and Z_{clo} is the closed loop output impedance of the Op-amp. The current gain A_v can be calculated as

$$A_v = \frac{I_{inj}}{V_a} = \frac{1 - G_{hpf}G_{amp}}{Z_{inj} + Z_{clo}} \tag{3.6}$$

which is frequency dependent. Among other things, A_v will depend on the Op-amp gain characteristics and the size of the injection capacitor. A larger capacitor will result in higher attenuation. However, in practical applications it will be limited as it adds to the total Y-capacitance.

An equivalent circuit of the Op-amp was presented in [30] and is shown in Figure 3.5. This model was used to derive G_{amp}, G_{hpf} and Z_{clo}.

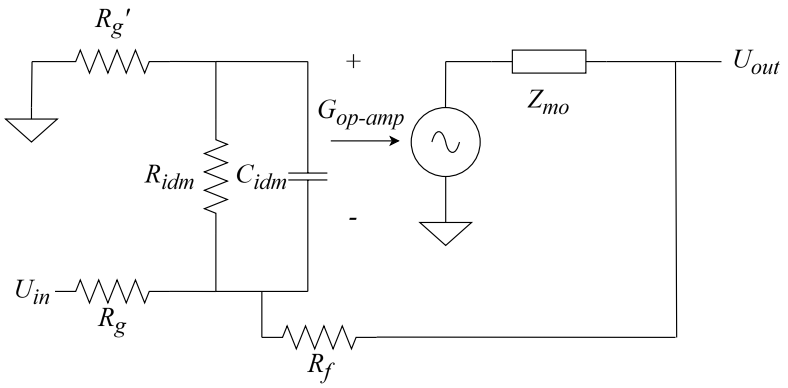

Figure 3.5: Op-amp circuit model [30].

Here, R_g, R_g' and R_f are the discrete resistors for controlling the gain of the amplifier, R_{idm} and C_{idm} are the input impedances, Z_{mo} is the output impedance and G_{op-amp} is the open-loop gain, simplified as

$$G_{op-amp} = \frac{G_0}{\left(1 + \frac{s}{\omega_1}\right)\left(1 + \frac{s}{\omega_2}\right)} \tag{3.7}$$

where ω_1 and ω_2 are the two poles of the Op-amp and G_0 is the open loop gain for DC. From the circuit model, the gain in the amplifier $-G_{amp}$ can be expressed as

$$-G_{amp} = \frac{G_{op\_amp} R_f}{\frac{2R_f R_g}{Z_{idm}} + (R_g + R_f + Z_{mo}) + G_{op\_amp} R_g}. \tag{3.8}$$

By introducing the internal pole at

$$\omega_{in} = \frac{1}{R_g C_{idm}} \tag{3.9}$$

the transfer function $-G_{amp}$ can be further expressed as

$$-G_{amp} = \frac{A_{op}}{1 + \frac{A_{op}(\omega_1 + \omega_{in})}{G_0 \omega_1 \omega_{in}} s + \frac{A_{op}(\omega_2 + \omega_{in})}{G_0 \omega_1 \omega_2 \omega_{in}} s^2 + \frac{A_{op}}{G_0 \omega_1 \omega_2 \omega_{in}} s^3} \tag{3.10}$$

where A_{op} is the amplification

$$A_{op} = \frac{R_F}{R_g + \frac{R_g + R_F}{G_0}} \tag{3.11}$$

which is a scaled version of the open-loop voltage gain G_0.

The closed loop impedance Z_{clo} was derived in [19] and is expressed as

$$Z_{clo} = \frac{Z_{mo}}{1 + \frac{Rg}{Rg+Rf} G_{op\_amp}} \tag{3.12}$$

where all parameters are described in Figure 3.5. Furthermore, the input impedance of the Op-amp Z_{in_amp} can be expressed as

$$Z_{in\_amp} = R_g + \frac{Z'_g + Z_{idm}}{(1 + G_{op_amp}) \cdot \frac{Z_{idm}}{R_f+Z_{mo}} + \frac{R'_g+R_f+Z_{mo}}{R_f+Z_{mo}}} \tag{3.13}$$

which can be used to calculate the gain G_{hpf} as

$$G_{hpf} = \frac{Z_{in\_amp}}{1 + Z_{in\_amp}} \approx \frac{s}{s + \omega_{hpf}} \tag{3.14}$$

The main parameters used for the calculations for the Op-amp OPA690 are given in Table 3.1 [7], [39].

Table 3.1: Parameters for OPA690 used in analytical calculations.

Parameter	Value	Parameter	Value
R_{idm}	500 kΩ	ω_1	80 kHz·2π
C_{idm}	0.1 pF	ω_2	300 MHz·2π
G_0	70 dB	Z_{mo}	20 Ω

3.5 Stabilization

In addition to analyzing insertion loss, the AEF's loop gain can be analyzed in order to understand the stability criterion. The filter's control diagram is presented in Figure 3.6.

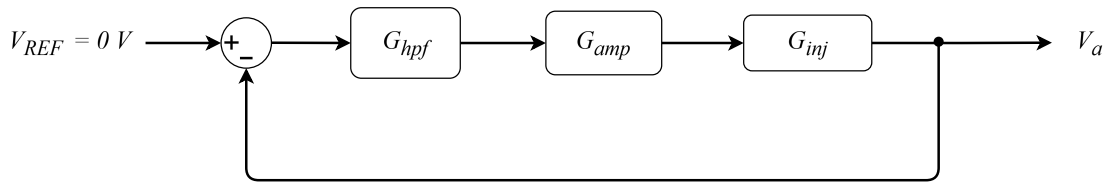

Figure 3.6: Control diagram of proposed filter.

Here, V_{REF} is a fictive quantity for the analysis, showing that the disturbance voltage should be 0 V and G_{inj} is the transfer function for the injection stage and is calculated as

$$G_{inj} = \frac{Z_{ol}}{Z_{inj} + Z_{clo} + Z_{ol}} \tag{3.15}$$

where Z_{ol} is the open-loop impedance, expressed as

$$Z_{ol} = \frac{(Z_n + Z_{L2})\,(Z_s + Z_{L1})}{(Z_n + Z_{L2}) + (Z_s + Z_{L1})} \tag{3.16}$$

here, the source Z_s impedance of the LISN. If it is assumed that the grid capacitance is very large, the impedance of the LISN can be simplified as

$$Z_{LISN} = \frac{sL_{LSIN}R_{LISN}}{sL_{LISN} + R_{LISN}} \tag{3.17}$$

For CM noise, two LISNs are connected in parallel. Therefore, $L_{LISN} = 2.5\,\mu\text{H}$ and $R_{LISN} = 25\,\Omega$. The noise impedance Z_n is normally the reactance of the remaining Y-capacitance in the product, measured to 60 nF in total of both lines.

From the control diagram, it is clear that the loop gain $L(s)$ can be expressed as

$$L(s) = G_{hpf}G_{amp}G_{inj}. \tag{3.18}$$

Thereafter, the closed loop gain $T(s)$ can be defined as

$$T(s) = \frac{L(s)}{1 + L(s)}. \tag{3.19}$$

In order to verify the model, the circuit was also simulated using LTspice. The loop gain $L(s)$ and the transfer functions G_{amp}, G_{hpf} and G_{inj} were plotted from the analytical model together with the loop gain from the LTspice simulation in Figure 3.7.

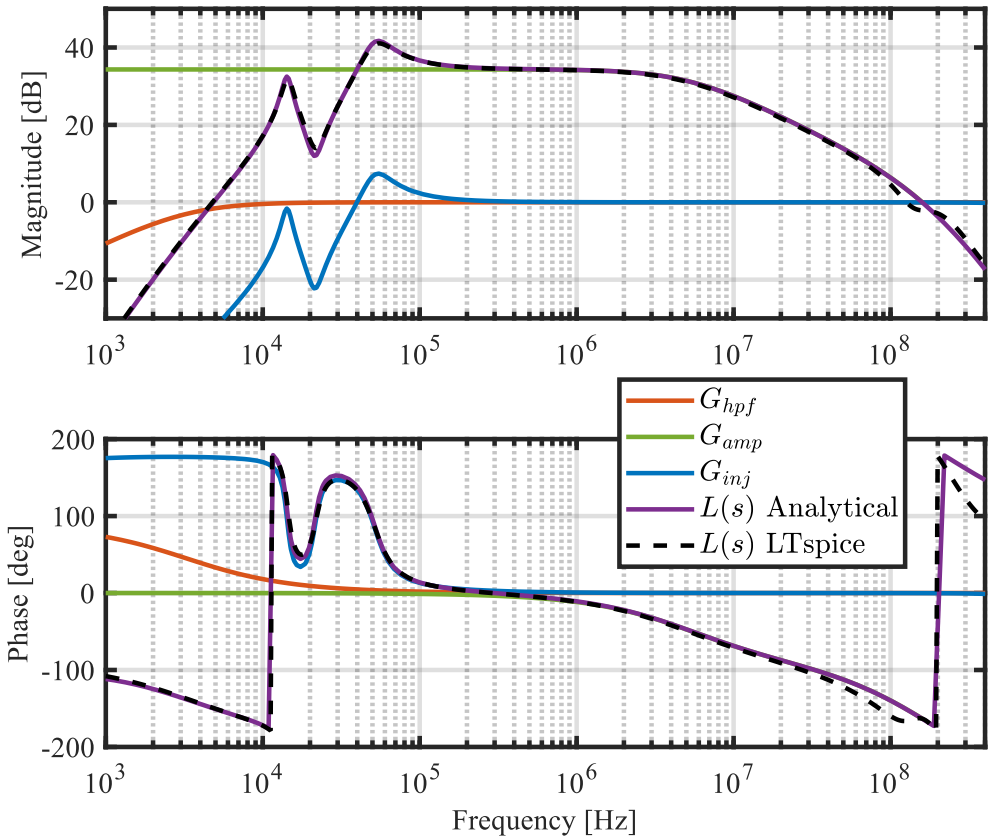

Figure 3.7: Loop gain and transfer functions G_{hpf}, G_{amp} and G_{inj}.

Figure 3.7 shows that different components contribute to the loop gain $L(s)$ shown in purple. The contributing factors are the amplifier gain G_{amp} shown in green, and the high pass filter gain G_{hpf} resulting from the sense capacitor is shown in orange. As the injection capacitor is a Y-capacitor and is limited due to safety considerations, the injection gain G_{inj} shown in blue cannot be altered.

G_{hpf} can be adjusted with the R_g resistor. By selecting a large resistor, the cutoff frequency ω_{hpf} becomes low and the phase is low near the zero crossing. This will however make the R_f very large to obtain the desired high gain, which can lead to high frequency instability due to the input capacitance of the Op-amp.

At both zero crossings of the loop gain, the phase margin is negative, leading to an unstable system. This is also shown with the step response of $T(s)$ given in Figure 3.8.

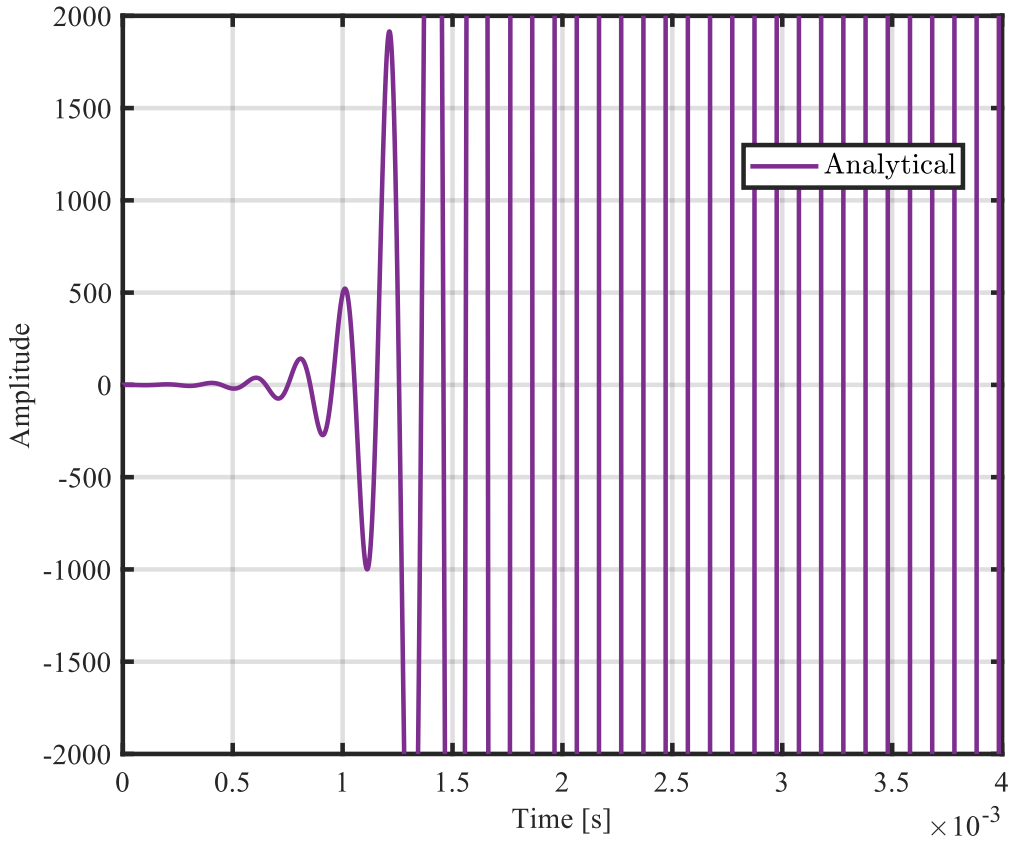

Figure 3.8: Step response of $T(s)$.

The step response in Figure 3.8 shows that the system is unstable.

3.5.1 Low Frequency Stability

According to the Nyquist stability criterion, sufficient phase margin φ must be obtained at the cutoff frequency where $|L| = 0\,\text{dB}$ [40].

As derived in [7], at the first zero crossing, the phase will be approximately

$$\angle L(s) = \angle G_{hpf}(s) + \angle - G_{amp}(s) + \angle G_{inj}(s). \tag{3.20}$$

At low frequencies,

$$\angle G_{hpf}(s) = \arctan \frac{\omega_{hpf}}{\omega} \tag{3.21}$$

$$\angle G_{amp} \approx 0° \tag{3.22}$$

$$\angle G_{inj} = \angle \frac{Z_{ol}}{Z_{inj} + Z_{clo} + Z_{ol}} \approx \angle \frac{Z_{cmc} + Z_s}{Zinj} \approx s^2 L_{cmc} C_s = 180° \tag{3.23}$$

leading to a total phase of

$$\angle T(s) = 180 + \frac{\omega_{hpf}}{\omega} \tag{3.24}$$

which makes the system unstable. This is also clear from Figure 3.7, where the phase crosses 180° after the 0 dB crossing. It is also clear that the low frequency stability margins will be less when the source capacitance is large. With a smaller capacitance, the inductor in the LISN is not shorted to ground, resulting in a lower phase. The worst case is when the source capacitance is infinite. This was realized in low voltage verification and simulation by a short circuit between ground and power lines on the source side, to ensure stable operation in the worst case condition.

A Lead-Lag filter can be added to the circuit to increase the phase margin at low frequencies [7]. The filter lags the phase with reduced magnitude, but later recovers the magnitude and phase to keep high gain and performance. The filter consists of two resistors R_1 and R_2 and two capacitors C_1 and C_2. The circuit of a Lead-Lag filter is shown in Figure 3.9.

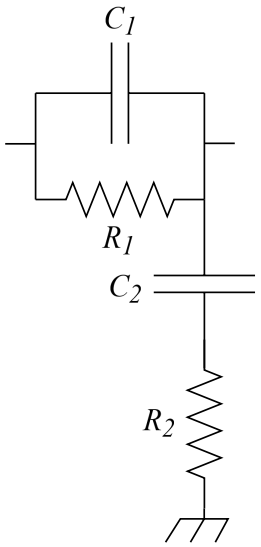

Figure 3.9: Components of a Lead-Lag filter.

The Lead-Lag filter in Figure 3.9 acts as a phase "Lag" that dampens the phase before increasing it, "Lead". The transfer function of the Lead-Lag filter G_{LL} can be expressed as

$$G_{LL} = \frac{s + \frac{1}{T_1}}{s + \frac{b}{T_1}} \cdot \frac{s + \frac{1}{T_2}}{s + \frac{2}{bT_1}}, \tag{3.25}$$

where the time constants T_1 and T_2 and the b coefficient are defined as

$$T_1 = C_1 R_1 \qquad T_2 = C_2 R_2 \qquad b = \frac{R_2}{R_1 + R_2}. \tag{3.26}$$

The Bode plot of the transfer function for a Lead-Lag filter is given in Figure 3.10.

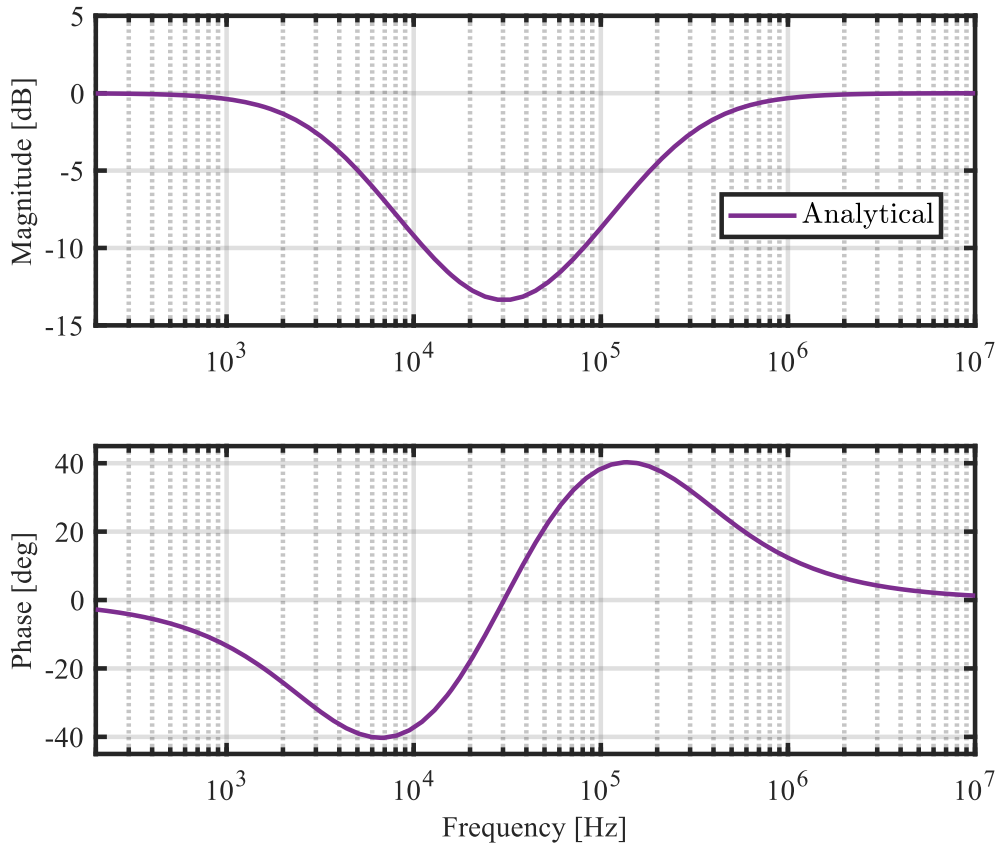

Figure 3.10: Transfer function of Lead-Lag filter.

As seen in Figure 3.10, the magnitude reduces when the phase "Lags" and increases when the phase "Leads". Note that the Lead-Lag filter will introduce a higher impedance in series with R_g which will affect the gain of the amplifier. The added impedance is a parallel connection of C_1, R_1 and $C_2 + R_2$. The impedance can therefore be calculated as

$$Z_{lead\_lag} = \frac{1}{\frac{1}{1/sC_1} + \frac{1}{C_1} + \frac{1}{R_2+1/C_2}} \tag{3.27}$$

which is plotted in Figure 3.11

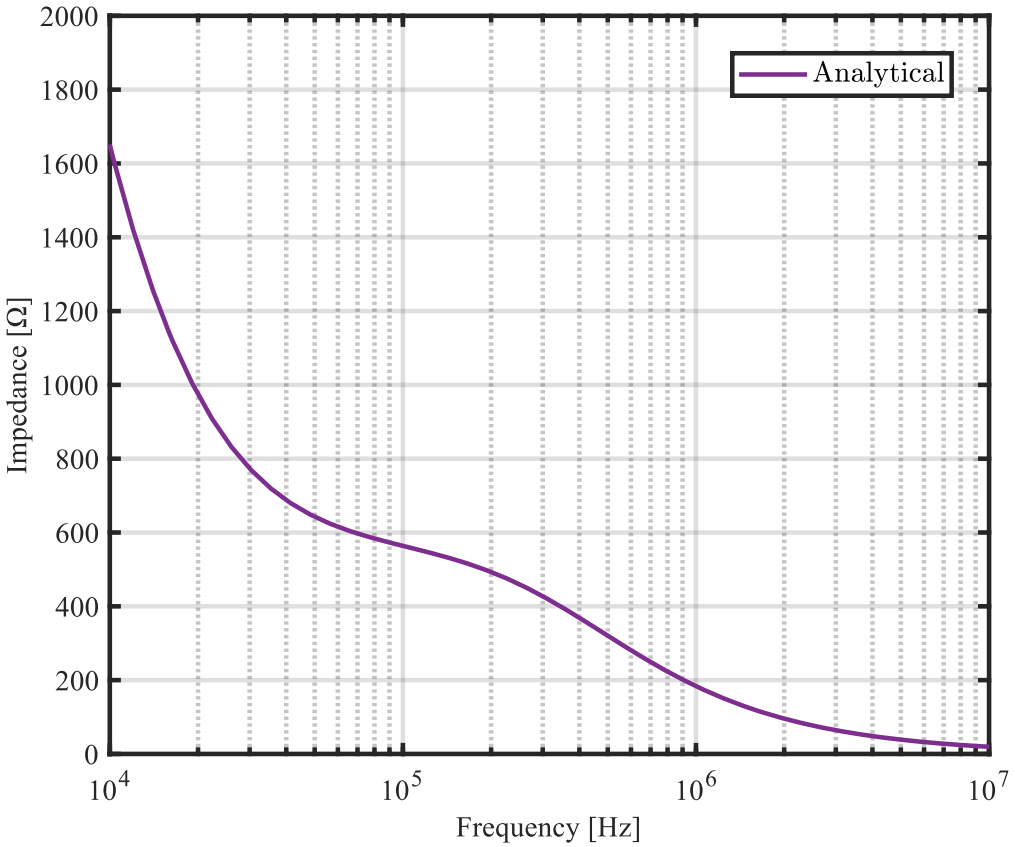

Figure 3.11: Impedance of Lead-Lag filter.

The impedance is 560 Ω at 100 kHz, which is less than 5.1 kΩ, producing a minor change to the gain. It is however necessary to include in the analytical calculations for an accurate loop gain and insertion loss.

The Lead-Lag filter can be introduced either before the amplifier as in [7], or after the amplifier [9]. One major drawback of placing the filter after the amplifier is that it increases the output impedance of the Op-amp, meaning that a larger voltage is needed to drive the same current in the injection capacitor, which lowers the performance of the filter. However, for very low disturbances, placing the filter at the sensing part will lead to more noise as the higher impedance makes the circuit more sensitive.

The filter parameters can either be calculated by assuming a width of the filter, a base resistor value and by selecting a frequency around the instability point [9]. It is however, hard to quantitatively design the filter for a specific phase margin and performance. Therefore, the parameters were swept in LTspice.

The simulation setup for the Lead-Lag parameter sweep was evaluated considering the worst case scenario. As previously described, the worst scenario for instability is when a large source capacitor is present. Therefore, the simulation was done with

a short circuit on the source side to emulate infinite capacitance. DC biasing of the ceramic capacitors in the filter could possibly also impact the stability margin. Therefore, the parameter sweep was done with the calculated DC bias in mind. The DC biasing at 700 V was provided by a previous measurement. The DC loaded capacitors at 700 V between both power lines, forming approximately 350 V across the Y-capacitors, were previously measured to lose 40 % of their capacitance. This 40 % loss was considered in the simulations.

Table 3.2 presents the parameter values swept between for the Lead-Lag filter

Table 3.2: Values of parameters in the parameter sweep in LTspice.

	C_1	R_1	C_2	R_2
Sweep	110 pF to 80 nF	200 Ω to 20 kΩ	110 pF to 1.6 µF	10 Ω to 20 kΩ
Steps	10/decade	10/decade	10/decade	10/decade

The values in the Lead-Lag filter are taken from parameter sweeps, according to Table 3.2, in LTspice using the .STEP function for the four components making up the Lead-Lag filter. All combinations from the sweep were analyzed and the combination of values that resulted in the highest IL at 300 kHz while maintaining φ =25° stability was chosen. The IL was evaluated at 300 kHz, as this is the first harmonic of the expected square wave from the switching frequency of 100 kHz. φ =25° was considered enough margin since the worst case scenario is seldom the real operating condition. Since the Lead-Lag filter attenuation reduces the IL, a compromise between phase margin and performance was reached. Thereafter, the component values closest to the E12 standard were selected, which are presented in Table 3.3.

Table 3.3: Parameter value results from parameter sweep in LTspice.

C_1	R_1	C_2	R_2
820 pF	5.6 kΩ	8.2 nF	680 Ω

The values for the Lead-Lag parameters presented in Table 3.3 were the final values mounted on the input of the AEF and were used throughout the rest of the thesis.

3.5.2 High Frequency Stability

At high frequencies,

$$\angle G_{hpf} = 1 \tag{3.28}$$

G_{inj} will depend heavily on the impedance of the CMC, which for high frequencies will be capacitive. Therefore, $\angle G_{inj} \approx \angle \frac{Z_{cmc,c}}{Z_{inj}} \approx 0°$. Therefore, the angle of the closed loop gain is

$$\angle T(s) = \angle - G_{amp}(s). \tag{3.29}$$

As the amplifier has zero zeros and three poles, it could be below 180° and become unstable. It is also possible that stray elements in the PCB give high frequency instabilities, especially as the very high resistor values in the feedback of the Op-amp create a pole with the input capacitance of the Op-amp. Therefore, a high frequency stability compensator is needed. From Figure 3.7, the phase margin at high frequencies is positive, meaning that the system is stable. The margins are however very small, meaning that some compensation is needed to make sure that the system is stable for all operating conditions and component variations. In addition, during the first measurements of the loop gain before any high frequency instability compensation, the AEF had a negative margin, which is presented in Figure 3.12.

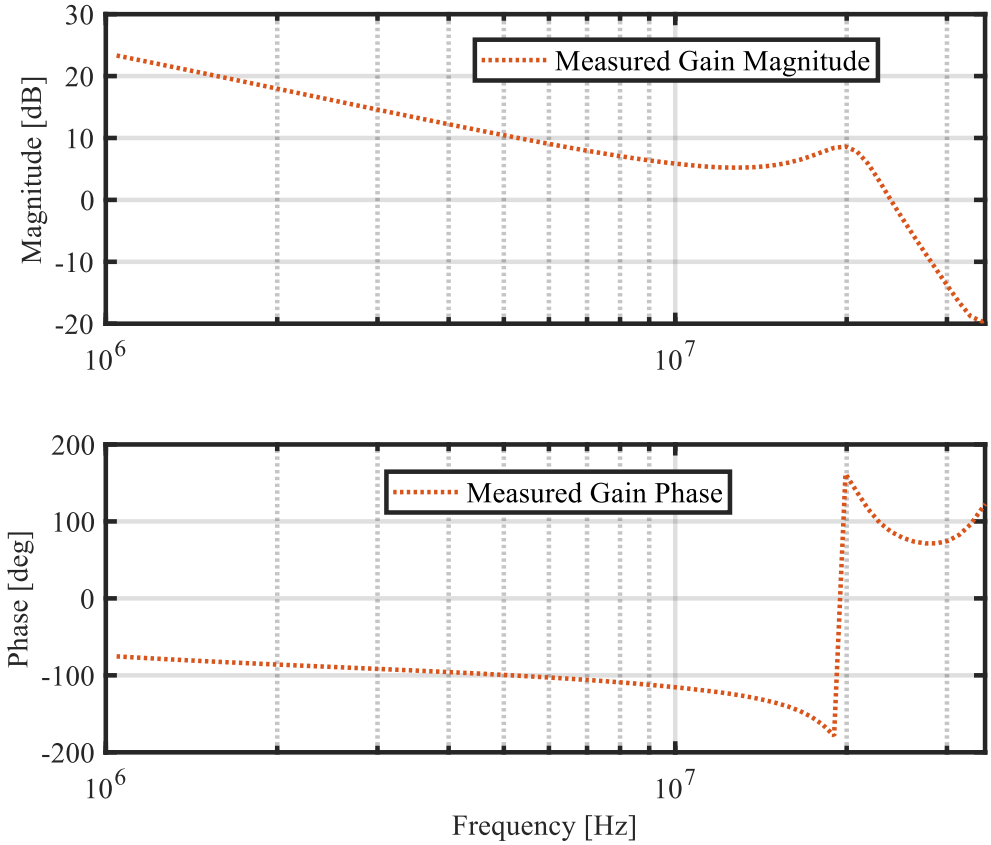

Figure 3.12: Measured loop gain before any high frequency stabilization was implemented.

A loop gain measurement shown in Figure 3.12 confirms the instability as the phase crosses −180° at approximately 20 MHz. A larger feedback capacitor to limit the bandwidth of the amplifier and a resistor to reduce the magnitude peak were needed in order to stabilize the AEF. The reduction in bandwidth reduces performance at higher frequencies, and the added resistor slightly reduces performance across the whole frequency range. In Table 3.4, the values implemented to stabilize the high frequency oscillations are presented.

Table 3.4: Parameters for high frequency instability mitigation.

Parameter	Value
C_f	4.7 pF
R_s	3.2 Ω

The capacitor value in Table 3.4 was implemented as a feedback capacitor to limit the bandwidth, and the resistor was implemented as a series resistor at the Op-amp output to reduce the peak at 20 MHz. During the verification, multiple Op-amps were used. One of them, the LT1818, needed a higher series resistance of 7.0 Ω to reach stability. The results from stability verification using $L(s)$ measurement are presented and further analyzed in the Analysis chapter.

3.6 Proposed Filter and Implementation

The total available capacitance $C_{sense} + C_{inj}$ is, as previously mentioned, strictly limited to 37.6 nF. For high insertion loss, a large proportion of the available capacitance should be allocated to C_{inj}. As also discussed previously, a low cutoff frequency ω_{hpf} of the sensing stage is needed for stability, implying that the product of R_g and C_{sens} should be as large as possible. However, a large C_{sense} gives a low C_{inj} which leads to a lower insertion loss. On the other hand, a too large R_g requires an even larger R_f to keep the gain high, which is practically unfeasible, as it makes the circuit sensitive to EMC and increases the noise. A compromise was reached with R_f selected to 270 kΩ and R_g selected to 5.1 kΩ to keep a gain of approximately 50. In order to be stable, a cutoff frequency lower than 0.1·150 kHz is desired as it results in almost 0° phase shift at the start of the measuring range at 150 kHz, as it is a first order low pass filter. That results in a capacitance of 2 nF. For practical reasons, a value of 4.7 nF was selected to ensure the frequency was low enough and due to component availability.

A simplified schematic of the final implemented active filter is shown in Figure 3.13.

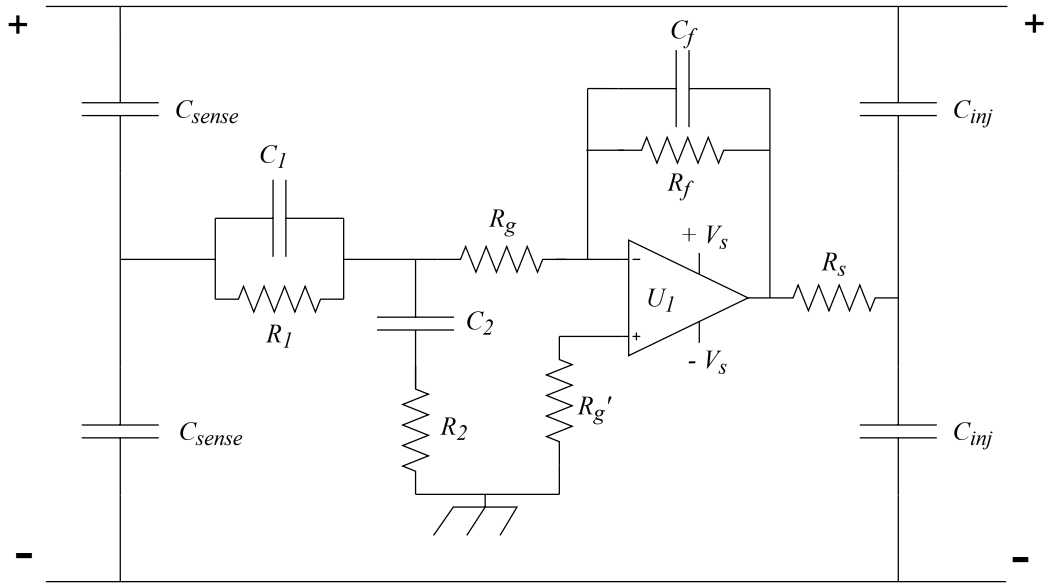

Figure 3.13: Simplified circuit of the AEF used for testing.

The two C_{sense} capacitors decouple the DC voltage and let the conducted AC emissions pass into the active filter. C_1, R_1, C_2 and R_2 make up the Lead-Lag filter for low frequency stability compensation. The capacitor and resistor C_f and R_f make up the gain and high frequency stability. R_s is also implemented for high frequency stability. The values of the parameters in Figure 3.13 are presented in Table 3.5.

Table 3.5: Component values in developed AEF.

Parameter	Value	Parameter	Value
C_{sense}	4.7 nF	R_g	5.1 kΩ
C_1	820 pF	R_g'	5.1 kΩ
R_1	5.6 kΩ	C_f	4.7 pF
C_2	8.2 nF	R_f	270 kΩ
R_2	680 Ω	R_s	3.2 Ω
V_s	4.5 V	C_{inj}	14.1 nF

Table 3.5 summarizes the values in the simplified AEF schematic used in the project.

The filter is realized with a prototype board built with a four-layer PCB. The full schematic of the built AEF prototype PCB is presented in Figure 3.14.

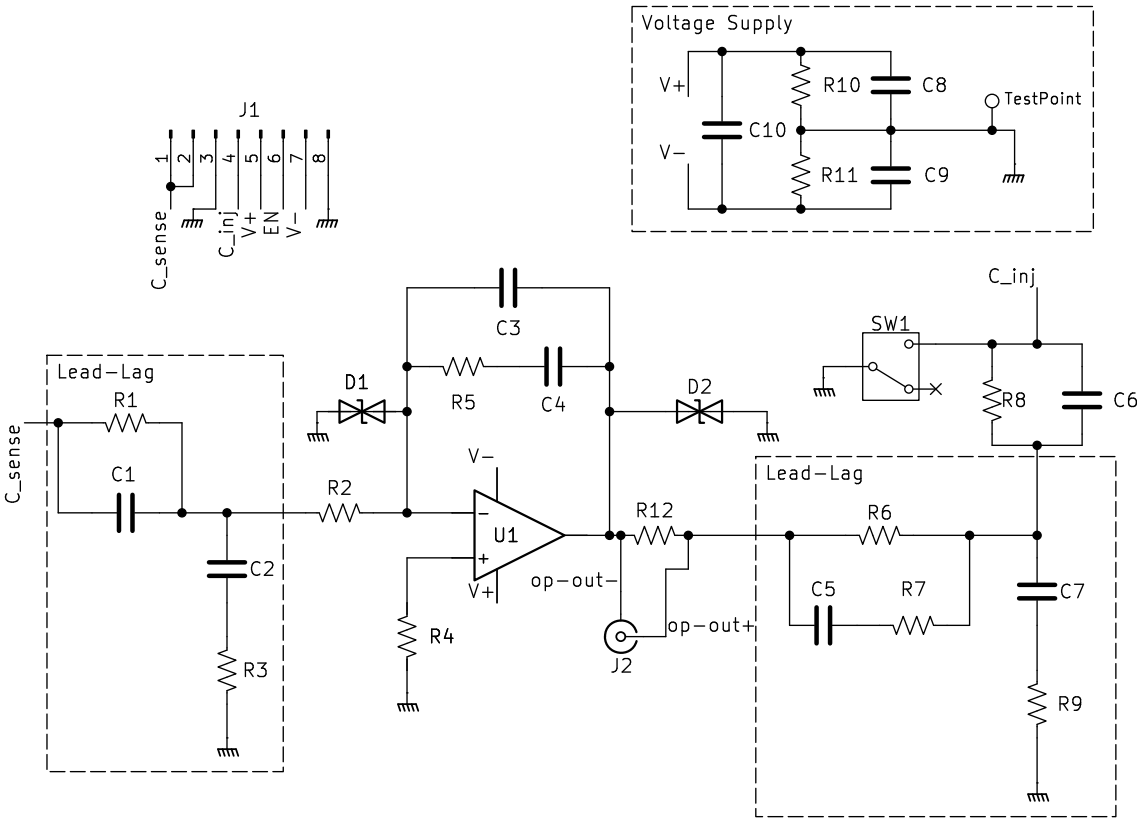

Figure 3.14: Full schematic of the built prototype PCB with the possibility of implementing a Lead-Lag filter on the input or output side.

Apart from the Active EMI Filter circuit in Figure 3.14, the board includes an MCX measurement port for output current measurement of the Op-amp through a $1\,\Omega$ shunt. The board also includes a GND test point for easy ground connection with probes and a switch that enables grounding of the injection capacitors. This switch effectively bypasses the active circuit and makes the filter passive. This grounding is, however, only for development purposes and was not used in the passive performance measurements, as it excludes the sensing capacitor and adds paracitics from added traces.

Empty pads are added to allow for relocation of the Lead-Lag filter to either before or after the Op-amp. Note that the Sensing and Injection capacitors are not mounted on the PCB, as the majority of the voltage drop will fall across them. This ensures no high voltages are present on the developed prototype board.

Additional components for the voltage supply of the Op-amp are also mounted. The circuit is powered with an external 9 V battery, that is connected between $V+$ and $V-$, which are centered around the ground potential with the capacitive and resistive voltage divider from R_{10}, R_{11}, C_8 and C_9. To avoid ripple, a capacitor was placed close to the voltage inputs of the op-amp to reduce the ripple.

The Bill of Materials (BOM) for the complete circuit of the developed PCB is presented in Table 3.6.

Table 3.6: Bill of Materials for the developed prototype AEF PCB.

Reference	Value	Description
R1	5.6 kΩ	Part of input Lead-Lag filter
R2	5.1 kΩ	Input resistor to Op-amp
R3	680 Ω	Part of input Lead-Lag filter
R4	5.1 kΩ	Bias resistor to ground
R5	270 kΩ	Feedback resistor
R6	Short (0 Ω resistor)	Part of output Lead-Lag filter
R7	Not mounted	Part of output Lead-Lag filter
R8	2.2 Ω	Part of output filter
R9	Not mounted	Part of output Lead-Lag filter
R10	10 kΩ	Voltage supply network
R11	10 kΩ	Voltage supply network
R12	1 Ω	Current sense resistor
C1	820 pF	Part of input Lead-Lag filter
C2	8.2 nF	Part of input Lead-Lag filter
C3	4.7 pF	Feedback capacitor
C4	Short (0 Ω resistor)	Feedback capacitor
C5	Not mounted	Part of output Lead-Lag filter
C6	Not mounted	Part of output filter
C7	Not mounted	Part of output Lead-Lag filter
C8	4.7 µF	Voltage supply network
C9	4.7 µF	Voltage supply network
C10	220 nF	Voltage supply network
D1	D3V3L1B2WS-7	TVS Diode
D2	SM6T22CA	TVS Diode
U1	Multiple variants (SOT-23)	Operational Amplifier
J1	2.54 mm pitch	8-pin connector header
J2	MCX-J-P-H-ST-SM1-TR	MCX contact
SW1	EG1218	Switch (SPDT)
TestPoint	5001	Ground Test Point

Table 3.6 declares all the needed components for the developed AEF PCB. Note that some components are not mounted and some pads are shorted. This was done to enable modifications after the production of the PCB.

The passive components are mostly size 0603. A current measurement MCX connector, a test point and a toggle switch were added for debugging purposes, which adds significant area to the PCB. It is therefore slightly larger than the TI EVM, measuring at 25 mm × 30 mm compared to the EVM at 25 mm × 20 mm.
The AEF prototype board is shown in Figure 3.15.

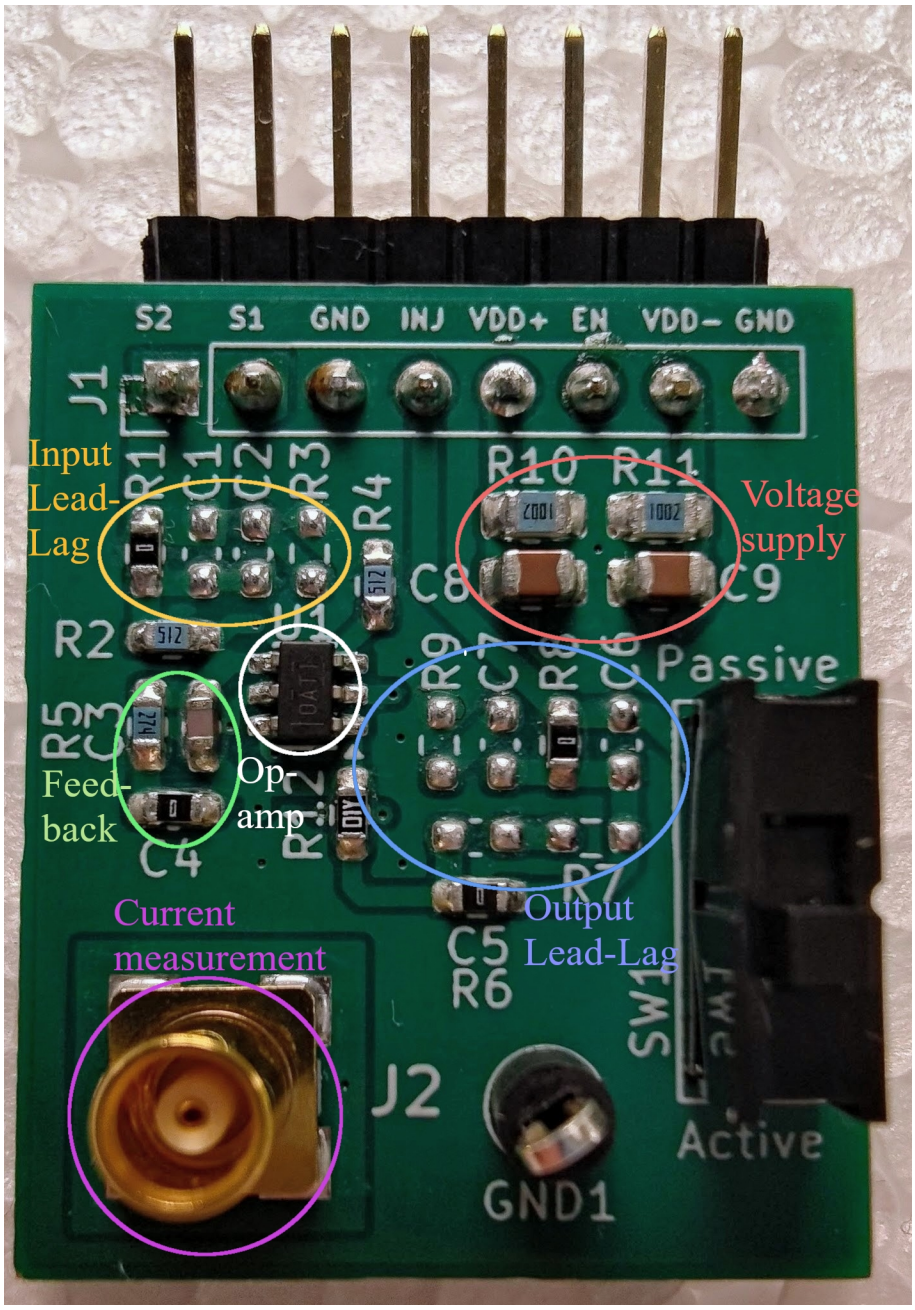

Figure 3.15: Developed prototype AEF board with different circuit functions marked.

The developed prototype AEF in Figure 3.15 has a similar circuit layout as the Texas Instruments EVM. The main components responsible for different circuit functions are marked in Figure 3.15. Note that the TVS diodes and capacitor C10 are mounted on the bottom side. The sensing and injection capacitors are not mounted on the developed PCB. These capacitors are instead mounted directly to the voltage rails on the passive filter PCB.

3.7 Texas Instruments IC

The IC TPSF12C1 from TI is a standalone AEF for CM mitigation and works for both AC and DC applications. The chip was evaluated with the EVM. The EVM has a similar structure as the developed chip and a filter for low frequency stability needs to be adjusted for the specific application. As written in the User Guide [32], TI has a quick start calculation tool for selecting appropriate filter parameters for the application, based on parameters such as grid and load impedance, CMC characteristics and the size of the sensing and injection capacitors. The circuit is given in Figure 3.16.

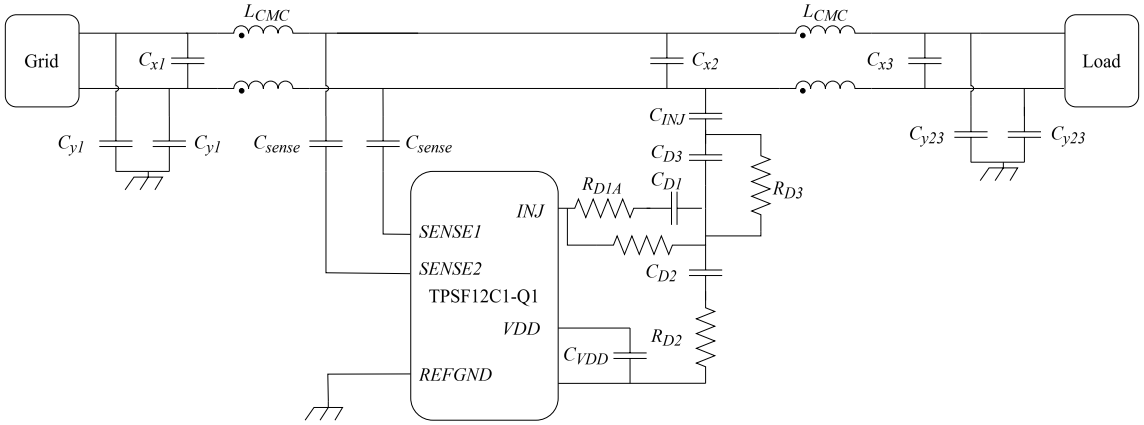

Figure 3.16: Overview of TI IC AEF circuit.

The CMCs, C_{y1},C_{y23},C_{x1},C_{x2},C_{x3},C_{sense} and C_{INJ} are the same as the circuit with the implemented AEF. The rest of the components in Figure 3.16 are given in Table 3.7.

Table 3.7: External parameter values for TI EVM calculated using the calculation tool and the values implemented.

Parameter	Calculated	Implemented
R_{D1}	1 kΩ	1 kΩ
C_{D2}	52 nF	45 nF
C_{D1}	5.6 nF	5.6 nF
R_{D2}	125 Ω	120 Ω
R_{D1A}	50 Ω	47 Ω
R_{D3}	700 Ω	700 Ω
C_{D3}	21 nF	33 nF

Table 3.7 shows the calculated values from TI's calculation tool. The implemented parameters are also presented. Overall, the circuit is similar to the proposed Op-amp based AEF. It uses the same topology (VSCI) and a similar sensing and injection stage. The biggest difference is that the Lead-Lag filter is placed at the output of the filter instead of at the input. This makes it important to keep the impedance as low as possible, in order to avoid a too high voltage drop across it.

4
Case Setup

In this chapter, methods for stability and performance verification are presented. First, the selected Op-amps and the test cases are presented, followed by all verification methods. Initially, the stability was verified with low voltage measurements, followed by a low voltage performance verification. Finally, the EMI emissions were measured with 700 V and at 20 kW.

4.1 Comparison Cases

For the developed active filter, four different Op-amps will be compared in all measurements. Note that all Op-amps have the same footprint using the SOT-23 package with the same pin layout. The Op-amps can therefore be interchanged on the developed prototype PCB. Some key specifications of the Op-amps used in the comparison are listed in Table 4.1 [41], [42], [43], [39].

Table 4.1: Op-amps specifications.

Op-amp:	LT1818	LT1815	LT6200-10	OPA690
Maximum Supply Voltage	±6.3 V	±6.3 V	±6.3 V	±6.5 V
Gain Bandwidth Product	400 MHz	220 MHz	1.6 GHz	300 MHz
Short-Circuit Current	±70 mA	±70 mA	±90 mA	±250 mA
Output Swing	±4.1 V	±4.1 V	±4.9 V	±3.9 V
Slew Rate	2500 V/µs	1500 V/µs	340 V/µs	1900 V/µs
Unity Gain Stable	Yes	Yes	No	Yes

All specifications listed in Table 4.1 are defined at ± 5 V supply voltage. As the implemented voltage supply in the developed AEF supplies the Op-amps with ± 4.5 V, the specifications, especially for Output Swing, are expected to be slightly reduced as the Rail-to-Rail headroom is slightly less.

In order to reduce the number of test cases, OPA690 was selected as the baseline for all other comparisons, as it has a large output current and has been shown to work well in AEF applications in previous studies [7]. OPA690 was compared to the passive filter to analyze the performance of the active filter compared to the existing passive filter. As there is not enough time to design a new smaller passive filter, the smaller filter is analyzed by unwinding turns in the CMCs to get lower inductance. OPA690 with 5, 4 and 3 turns in the CMCs were compared to the passive filter with 5 turns, to understand how much the inductance and size can be reduced for an AEF

with the same performance as the passive filter. As the inductance is proportional to the square of the number of turns, the size will decrease with

$$\eta = 100\left(1 - \left(\frac{N_2}{N_1}\right)^2\right) \tag{4.1}$$

percent when the number of turns decreases from N_1 to N_2.

4.2 Measurements and Verification

This section presents the methods used for measurements and verification of the different filters.

4.2.1 Low Voltage Stability Verification

The loop gain was measured with the Bode 100 using the gain measurement. The sensing capacitors were desoldered from the passive filter PCB and connected between the output and Receiver 1 ports of the Bode-100 and the injection node of the AEF. Receiver 2 was connected to the power lines after the output capacitors. The connection is shown in Figure 4.1.

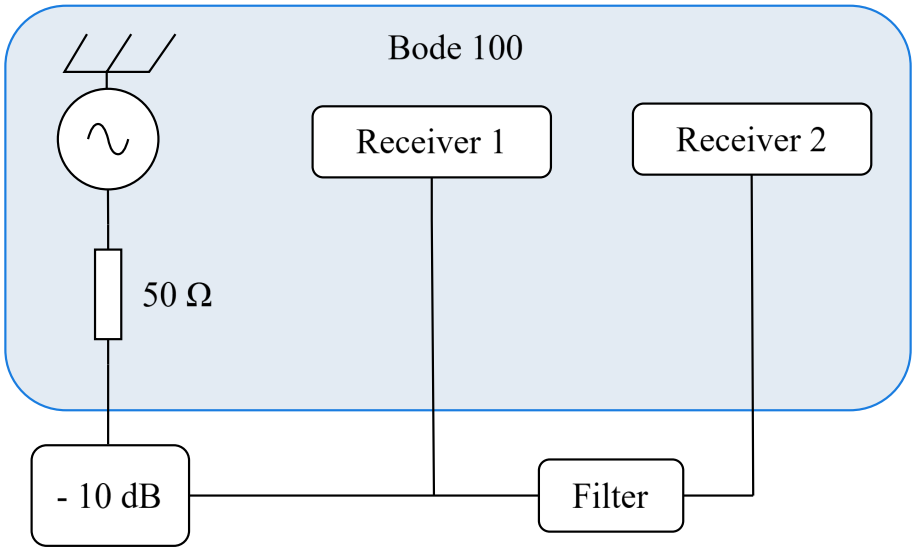

Figure 4.1: Low voltage loop gain measurement with Bode-100.

In order to use accurate impedance in the output and input of the filter, the measurements were done with the filter board mounted in the DC/DC converter. The DC/DC converter was placed on a styrofoam plate on a large ground plane inside an EMC chamber, the same setup as in CISPR 25 [17]. The worst case grid impedance was obtained by short circuiting both inputs to ground at the input of the LISN to act as a very large capacitance.

As the measurements are done with low voltage, the capacitors do not have any DC bias. To get a good understanding of the situation, the loop gain was simulated

with and without any DC bias and was verified by comparing the results with the measurement. After verifying the simulation, the loop gain was simulated with a DC bias to verify stability margins.

4.2.2 Low Voltage Performance Verification

The first physical performance verification measurement was performed with low voltage. The Bode-100 instrument was used to measure IL through the S_{21} scattering parameter according to [44]. During the measurement, 50 Ω terminations were used on both the sending and receiving ends to make the measurement reproducible and comparable. This measuring setup may not be a good representation of the performance in the actual product, as the external impedance will vary a lot. It is however, still preferred as it makes measurements easy to perform and comparable between other measurements and simulations. The test setup is presented in Figure 4.2.

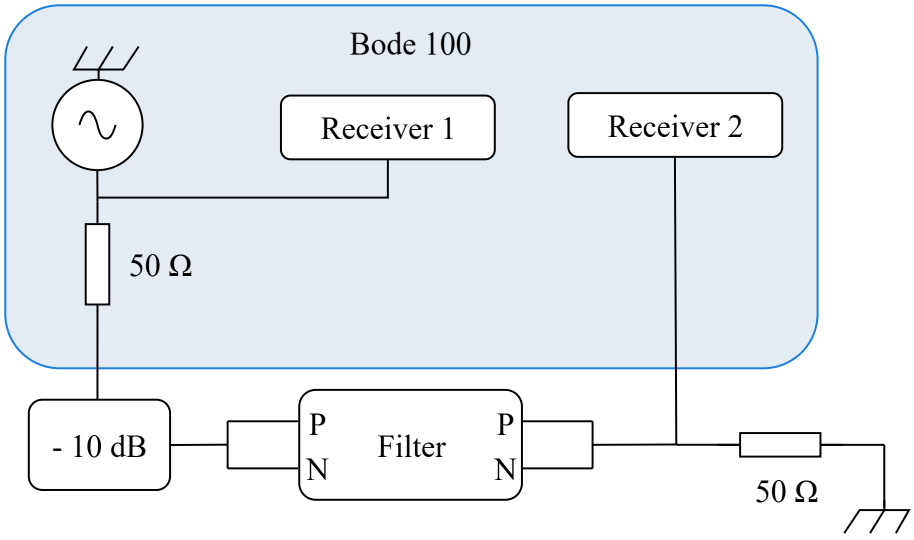

Figure 4.2: Low voltage insertion loss measurement setup.

As in Figure 4.2, at both the sending and receiving side, the positive and negative conductor was short circuited and the bode 100 cables were connected between the power conductors and chassis ground.

The filter board was not mounted in the DC/DC converter for the test. The filter board and chokes were placed in a plastic chassis which is normally surrounded by a ground plane in the DC/DC converter. To mimic the ground, the plastic chassis was covered in aluminium foil and placed on a 5 cm thick styrofoam plate on a large ground plane in an EMC chamber. To ensure minimizing of parasitics from cables, BNC contacts were soldered close to the filter.

The Bode-100 output port is limited to 5.0 V, but it is not recommended to apply more than 3.3 V [36]. As there is a risk of instability for the active circuit, there is

a risk that the active filter injects a voltage to the output of the Bode-100 larger than the maximum 5 V. Therefore, there is a need for attenuation to protect the instrument. As it is essential to keep the source and load impedance at 50 Ω, a Tee attenuator was built, which attenuates the signal, but does not affect the impedance. The Tee setup is illustrated in Figure 4.3.

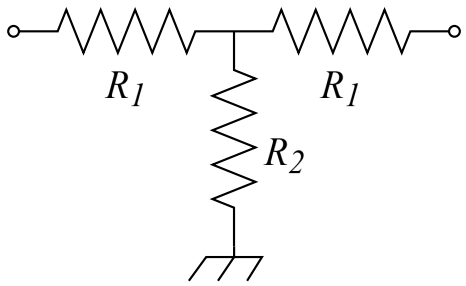

Figure 4.3: Tee attenuator that maintains impedance.

The resistor values in the Tee attenuator in Figure 4.3 are governed by the amount of attenuation and impedance desired [45]. The resistor values are calculated as

$$R_1 = Z_0 \left[\frac{10^{\frac{dB}{20}} - 1}{10^{\frac{dB}{20}} + 1} \right] \tag{4.2}$$

$$R_2 = 2Z_0 \left[\frac{10^{\frac{dB}{20}}}{10^{\frac{dB}{10}} - 1} \right] \tag{4.3}$$

[45], where Z_0 is set to the desired impedance of 50 Ω and the attenuation dB is set to 10. This results in resistors $R_1 = 26\,\Omega$ and $R_2 = 35\,\Omega$. The second receiver was terminated with 50 Ω outside of the Bode-100 in order to use the high impedance setting. As the high impedance setting can handle much higher voltages, there is no need for an attenuator, which gives a higher signal and less noise in the Bode 100.

4.2.3 High Voltage Performance Verification

After the low voltage verification, the AEF was evaluated in the EUT operating at the nominal voltage and power of 700 V and 20 kW. The measurement was carried out according to the CISPR 25 test standard in an EMC chamber. The test setup is presented in Figure 4.4.

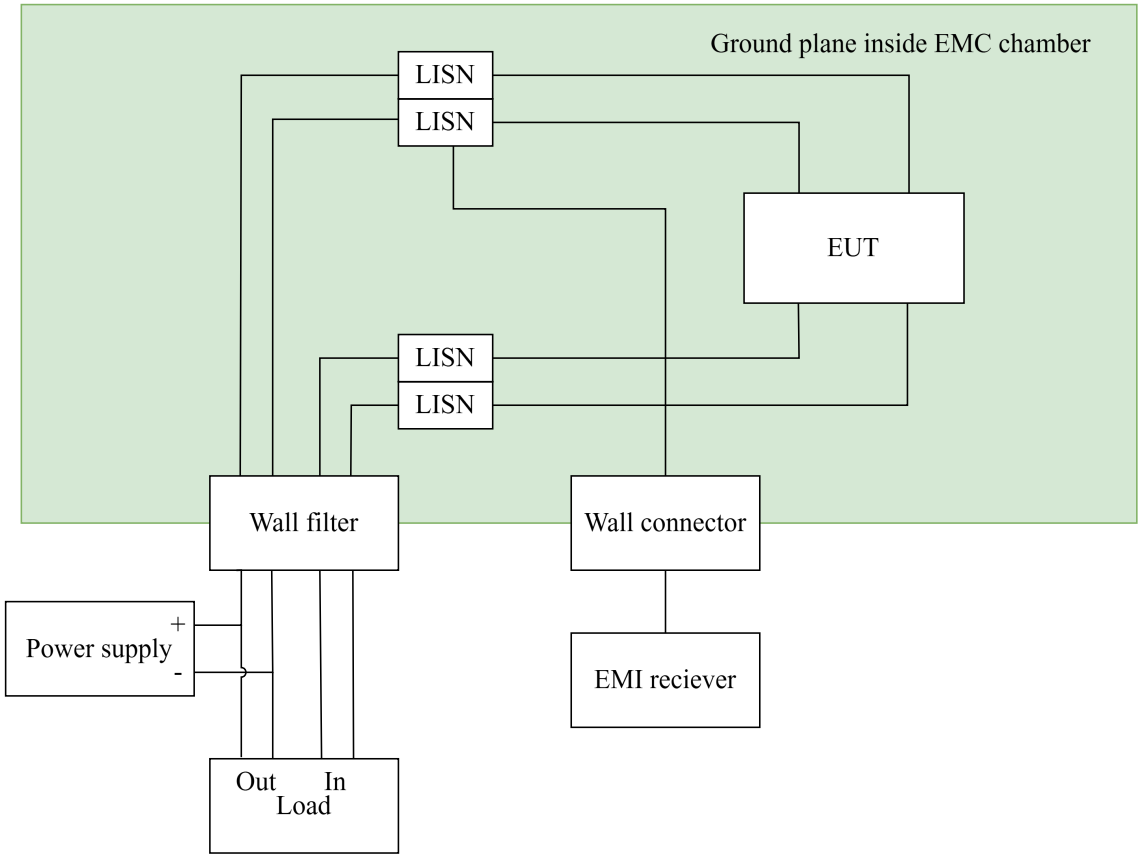

Figure 4.4: High voltage performance verification measurement setup.

The converter was placed on a styrofoam plate, 50 mm above the ground plane. Four CISPR 25 compliant LISNs were connected to the positive and negative input and output of the converter with 200 cm long cables. The output was fed to another bidirectional DC/DC converter that acted as a load, which fed back the energy to the input of the EUT. A high voltage DC supply was used to feed the remaining power from the losses in the EUT and the load. The CM EMI emissions were measured with an EMI receiver placed outside the EMI chamber. The EMI receiver was connected to the measurement port of the LISN on the positive side of the input, while the remaining LISN outputs were terminated with 50 Ω. In order to place the power supply and the load unit outside the EMI chamber, a wall filter was used to block high frequency content in and out of the chamber. For the signal, a wall connector was used to not interfere with the EMC chamber properties.

According to CISPR 25, the EUT housing ground lead should not be longer than 15 cm. However, due to the application of this specific DC/DC converter, a stricter requirement of 100 cm long ground cable was used.

In order to further characterize the EMI spectrum, a LISN MATE was used to separate the DM and CM disturbances. The output of both LISNs for the input was connected to the LISN MATE. One of the outputs of the LISN MATE was connected to the EMI receiver, while the other was terminated with 50 Ω. The three cases were measured from 150 kHz to 30 MHz for the passive filter and all active

filters. In addition, the passive filter and the AEF with OPA690 were measured with 4 turns in the CMCs to mimic the behavior of smaller CMCs.

In addition to measuring the EMI emissions, the output voltage and current of the Op-amp in the AEF were measured with an isolated oscilloscope.

5
Analysis

The following chapter presents and analyzes the results of this study. Initially, stability is verified, followed by the low voltage performance verification. After the initial verification, the filters are evaluated by measuring the EMI emissions from the DC/DC converter with various filter configurations. Finally, the size and power consumption, together with ethical and environmental aspects are analyzed and discussed.

5.1 Low Voltage Stability Verification

First, the simulation and analytical model of the loop gain are verified by comparing the results with measurements of the OPA690, followed by an Op-amp comparison. Then the implications of DC bias and the number of turns in the CMCs are analyzed.

5.1.1 Simulated and Measured Loop Gain

With the instability solutions for low and high frequencies, the stability can be analyzed by inspecting the loop gain $L(s)$ in Figure 5.1, where the loop gain from the analytical model, LTspice simulation and low voltage measurements of the AEF with OPA690 are provided.

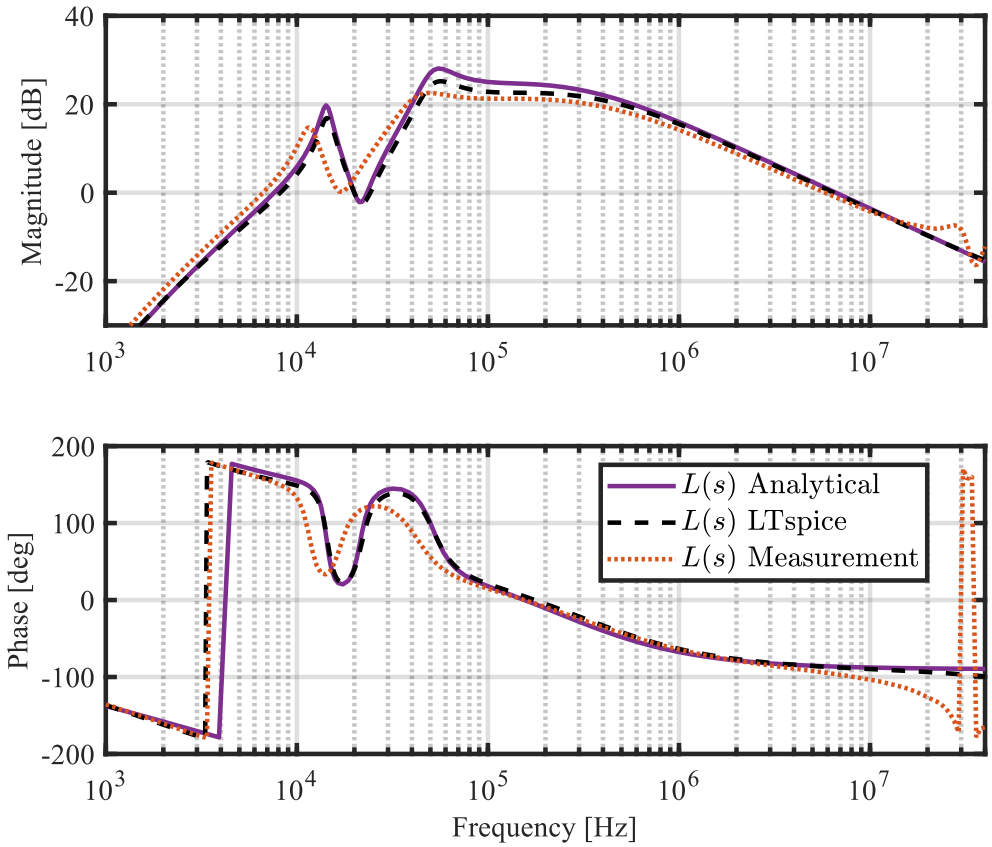

Figure 5.1: Simulated, modeled and measured loop gain.

Figure 5.1 shows that the simulation and the analytical model are good representations of the system, as the loop gain is similar to the measurements. The resonances have slightly lower frequency in the measurements, probably because there is more capacitance in the converter than considered in the models.

Furthermore, Figure 5.1 shows that the phase margin at low frequencies for the measurement is 23° and for the simulation and analytical model 26°. This is consistent with the designed margin, indicating that the stabilization is behaving as expected.

For high frequency, the simulation, model and the measurement have a phase margin of 88°. Note however, that the gain is slightly increasing near the 180° phase crossing, which gives 8.9 dB magnitude margin. Therefore, the margins can not be reduced much further. It may however be possible to optimize the bandwidth by reducing the resonance peak by increasing the series output resistance and thus allow for a lower feedback capacitor C_f which could increase the usable bandwidth. However, the increased impedance of the resistor would also lower the performance of the AEF, as it would lower the output current and increase the voltage drop. In addition, as will be clear in the next section, the bandwidth will in practice be limited to only 1 MHz, which implies that a larger bandwidth would not benefit the performance of the filter.

To further prove stability, the step response is given in Figure 5.2 where the closed loop gain $T(s)$ was calculated from both the analytical model and from the measured loop gain.

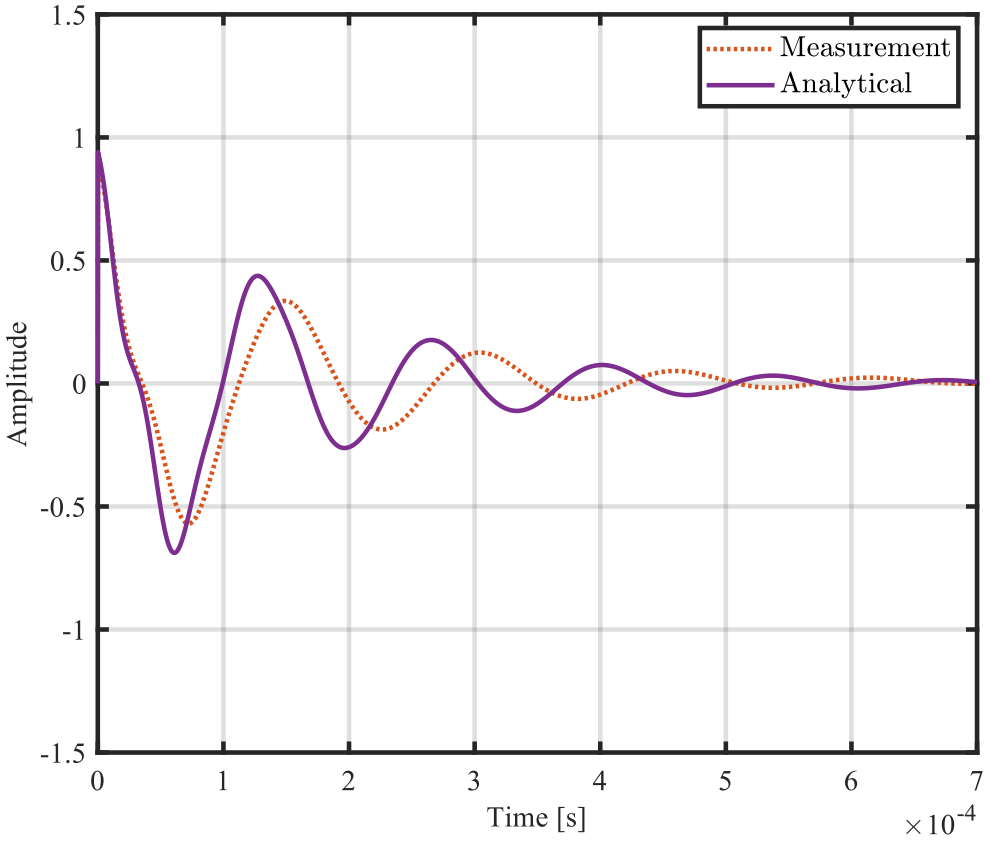

Figure 5.2: Step response of closed loop gain $T(s)$ after stabilization.

The step response in Figure 5.2 is a damped oscillation, which means that the circuit is stable. This is considered good enough in this case as the step is fully damped within 1 ms.

5.1.2 Op-amp Comparison

The loop gain was also measured for all Op-amps to ensure stability in all cases. As the loop gain mainly depends on the impedances in the passive filter and the bandwidth set by the C_f capacitor, it is expected to be the same for all Op-amps. The IC from Texas Instruments uses other stability methods and is expected to have a larger bandwidth. This was verified by measuring the loop gains of all Op-amps and the TI IC, which is presented in Figure 5.3.

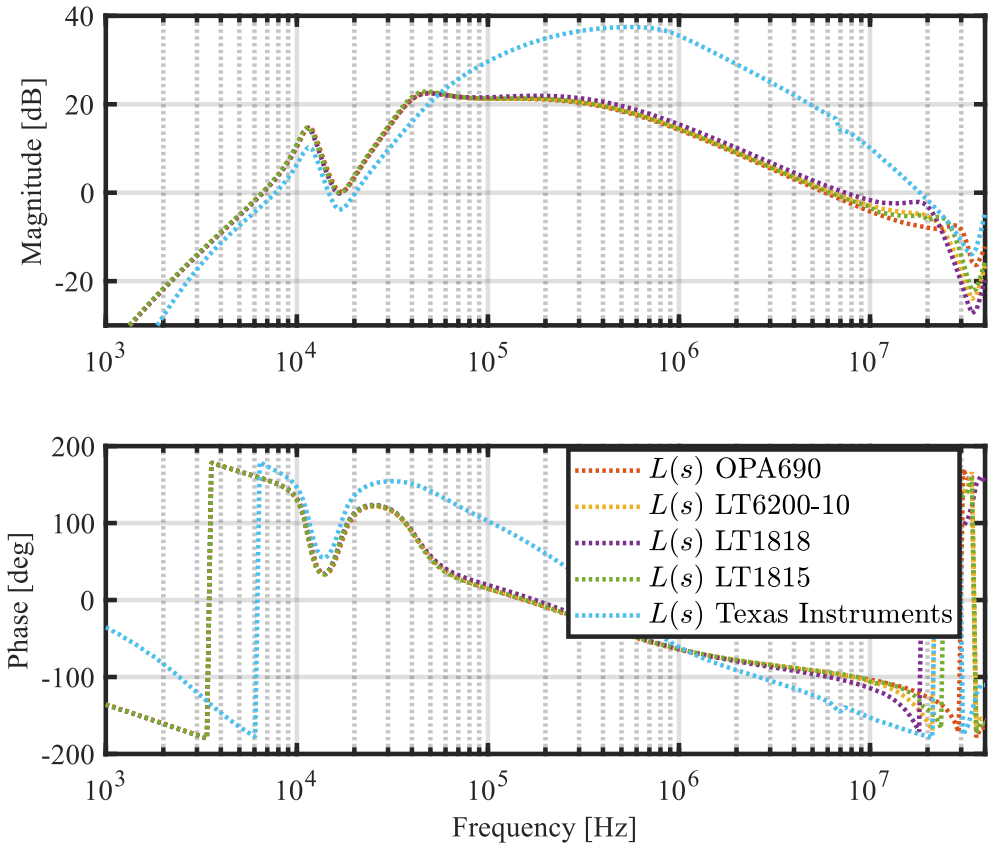

Figure 5.3: Loop gain for all AEFs.

As seen in Figure 5.3, all Op-amps give a similar loop gain, while the bandwidth of the TI IC is much larger.

5.1.3 Loop Gain Under DC bias

As it is tricky to measure the loop gain during DC bias, the gain was simulated in LTspice with capacitance calculated for DC bias. The simulated loop gain with and without bias, as well as the measured loop gain without bias are given in Figure 5.4.

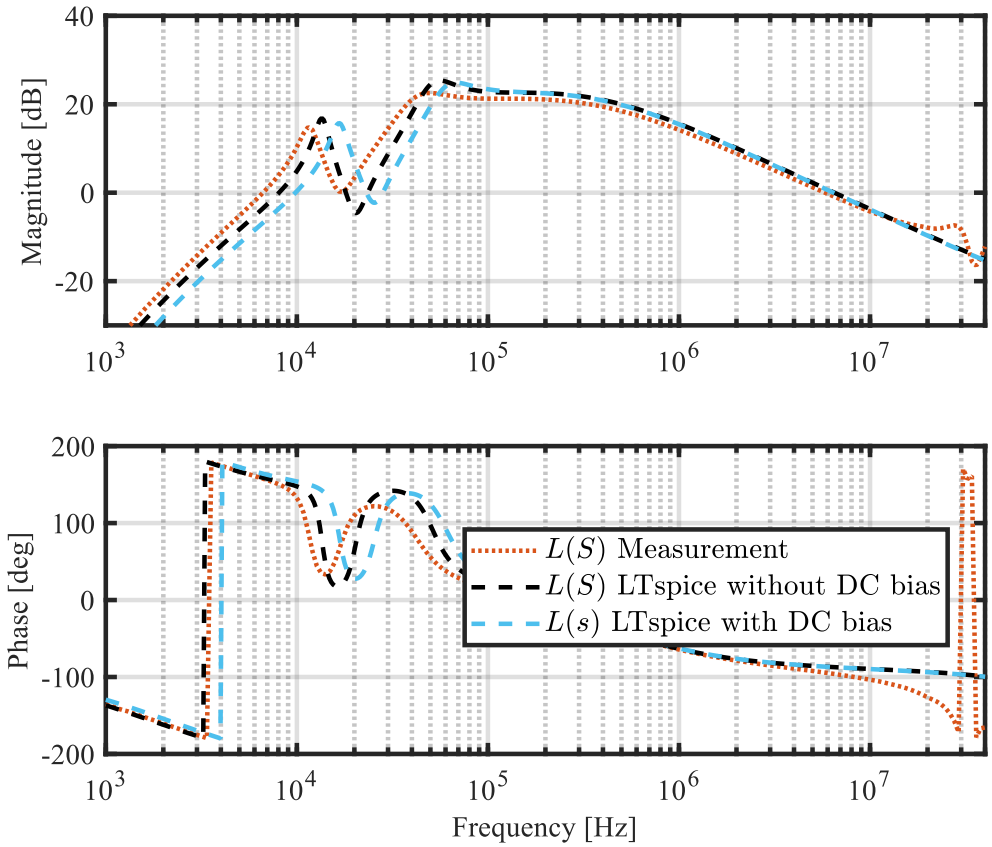

Figure 5.4: Simulated loop gain with and without DC bias.

In Figure 5.4, as the capacitance decreases, the corner frequency of the injection impedance increases. The phase shifts in a similar way. The resulting stability margin remains at 26°. Therefore, the AEF is likely to remain stable even during DC bias, even if it was not verified with measurements.

5.1.4 Loop Gain for Different Number of Turns in the CMC

To ensure stability with different numbers of turns in the CMCs, the loop gain was also measured for the OPA690 with 5, 4 and 3 turns in the CMCs, which are presented in Figure 5.5.

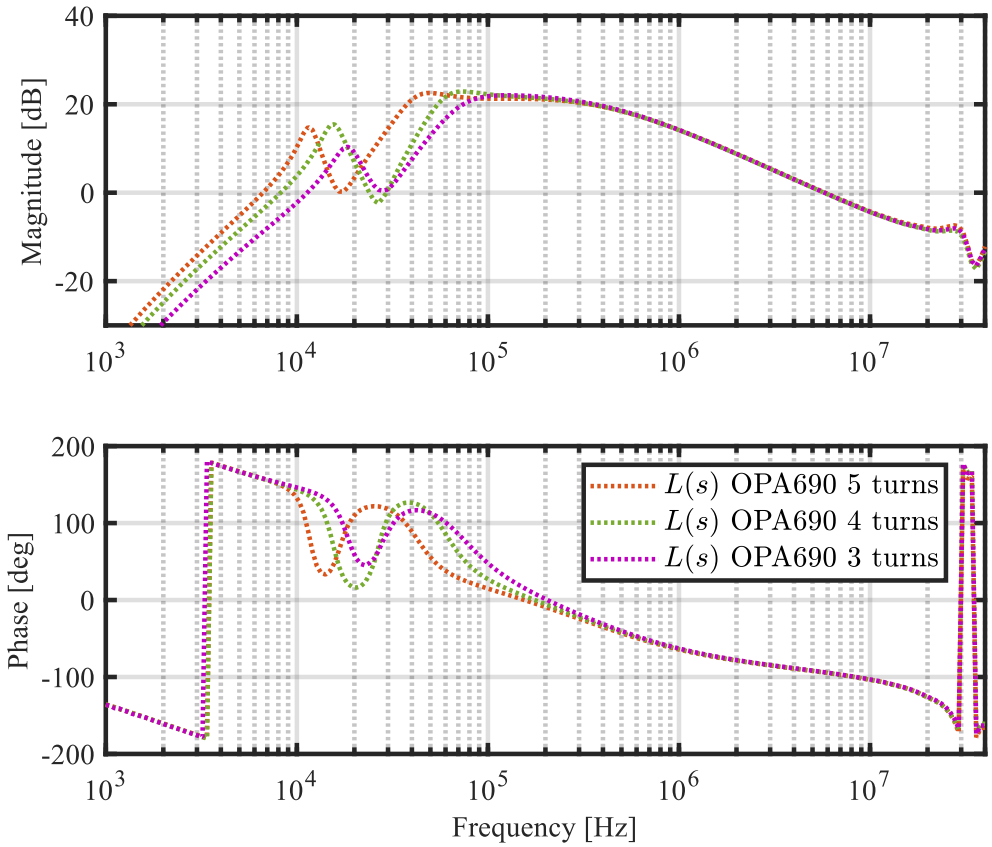

Figure 5.5: Loop gain for OPA690 with different numbers of turns in the CMCs.

Similar to the case of DC bias, a lower inductance from a lower number of turns in the CMC gives a higher cutoff frequency which returns higher stability margins, which is clear from Figure 5.5. However, the inductance does not affect the phase in the same way, which results in greater margins. The phase margin φ for different numbers of turns is given in Table 5.1

Table 5.1: Low frequency phase margin for different numbers of turns in the CMC.

Number of turns	Phase margin φ
5	23.1°
4	29.8°
3	37.95°

Table 5.1 summarizes the low frequency phase margins for different number of turns in each CMC. It is shown that the phase margin increases when the CMC turns decrease.

5.1.5 Stability Summary

In summary, it can be concluded that the Lead-Lag filter successfully established low frequency stability. The solution has also shown to be robust against DC bias as well

as different number of turns in the CMC. For high frequency instability, series output resistance for damping resonances in combination with parallel feedback capacitance to limit the bandwidth yields a good way of controlling stability margins.

5.2 Low Voltage Performance Verification

The performance of the EMI filters was initially verified by analyzing the IL of the filters. First, the model and analytical model were verified by comparing the results to the measurements. Thereafter, the different Op-amps and the TI IC were compared to the passive filter. Finally, the number of turns in the CMCs were varied for the AEF to understand how much the inductance can be lowered while performing similarly to the passive filter.

5.2.1 Simulated and Measured Insertion Loss

The insertion loss was measured, simulated and analytically calculated for the OPA690. An additional simulation was made with adjusted parasitics to get results closer to the measurements. The insertion losses are given in Figure 5.6.

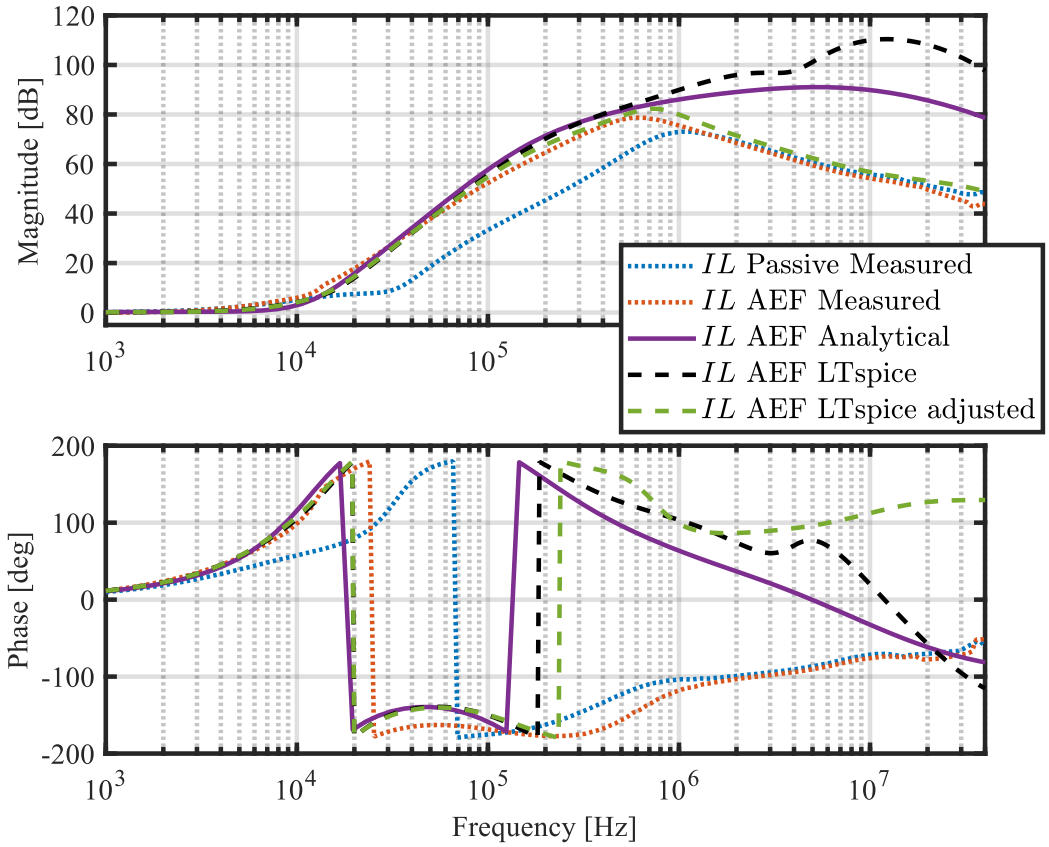

Figure 5.6: Analytical, Simulated and measured insertion.

During the measurements, the insertion loss of the AEF in Figure 5.6 was higher

than that of the passive filter in the frequency range 20 kHz to 1 MHz, which is the target frequency range. The low frequencies are the most important, as higher frequencies can be attenuated with smaller passive components. The model and simulation match for low frequencies, but deviated from the measurements after 1 MHz. An attempt to correct this behavior in simulations was made by placing a small bypass capacitor of 1 pF across the whole filter board, as well as adding a small inductance of 25 nH between the ground of the filter and the true grounding point. The adjustments improved the simulated insertion loss magnitude, but the phase is still wrong, suggesting that it may be other mechanisms or distributed parasitic elements contributing to the changes.

To further analyze why the filter stops performing after 1 MHz, a voltage measurement on the filter input, filter output and middle node (between the CMCs) was performed while injecting noise with different frequencies. The result is presented in Table 5.2.

Table 5.2: Voltages at the input, middle and output nodes at various frequencies.

		Passive Filter	AEF
300 kHz	Input	1307 mV	1232 mV
	Middle	34.57 mV	3.647 mV
	Output	8.357 mV	0.5961 mV
1 MHz	Input	515.0 mV	522.4 mV
	Middle	2.894 mV	0.8500 mV
	Output	0.8432 mV	0.6100 mV
10 MHz	Input	453.7 mV	471.8 mV
	Middle	0.9433 mV	2.969 mV
	Output	2.569 mV	4.913 mV

Table 5.2 shows that the 300 kHz signal behaves as expected. The active filter reduces the noise in the middle node and at the output by roughly a factor of 10. For the 1 MHz, the active filter reduces the noise with roughly a factor of 3.5, proving that it still works even if it is less effective. The voltage at the output node however, is not as affected, resulting in a very small difference in the insertion loss plot, even if the active filter is working. This indicates almost no attenuation between the middle and output node of the AEF and that the noise signal somehow bypasses this stage.

At 10 MHz, the voltage levels between the middle node and output node increase compared to the decrease for 300 kHz. This strongly suggests the noise signal has a path around the middle node, resulting in that the middle node damping has almost no effect. This is possibly due to stray capacitance in the PCB or other parasitics, implying that the noise signal bypasses the middle node. In that case, the performance of the EMI filter cannot be enhanced with higher Y-capacitance or an active filter in the middle node.

5.2.2 Op-amp Comparison

Similar to the stability analysis, all Op-amps are expected to have the same insertion loss, as the bandwidth and magnitude are controlled by the external components and not the Op-amp parameters. The IL of all active filters with the original 5 turns CMCs was measured and is plotted in Figure 5.7.

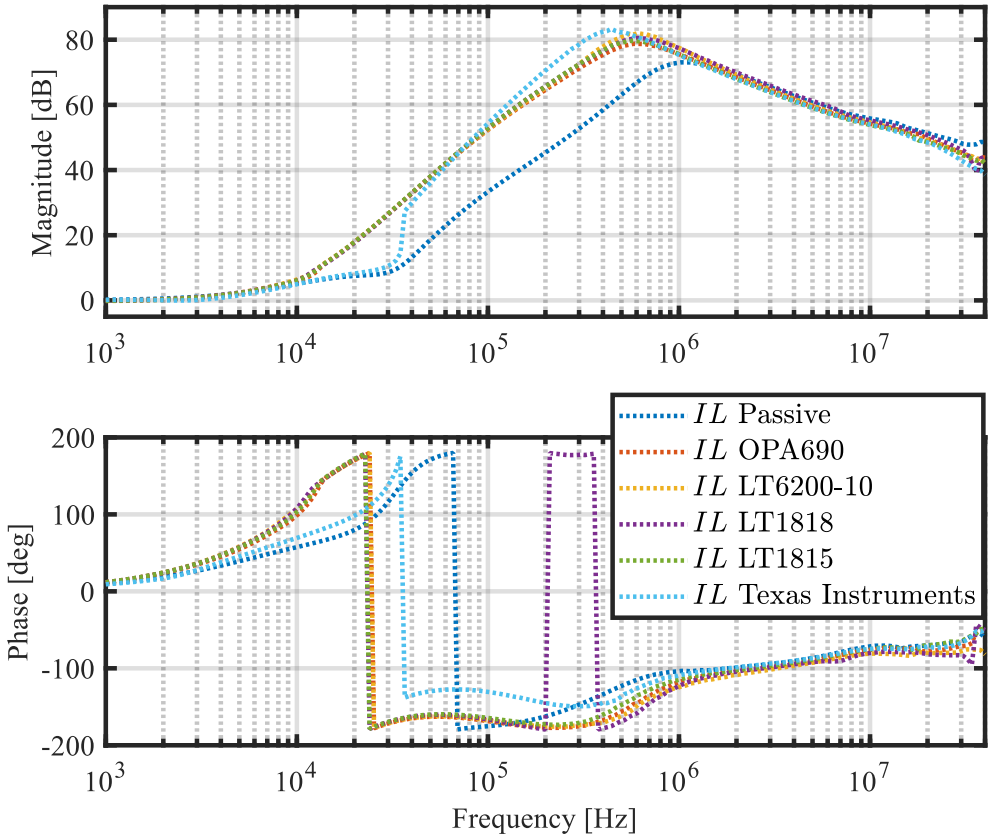

Figure 5.7: Insertion loss of all filters.

Figure 5.7 shows that all Op-amps implemented in the AEF perform better than the passive filter up to 1 MHz, from where all filters perform equally. As the insertion loss is controlled by the selected gain and bandwidth, all Op-amps are performing equally. For low frequencies, the TI IC is performing much worse, but the performance is good for high frequencies. This was further analyzed by measuring the voltage at the output of the IC, and at the injection node when the 30 kHz noise signal was applied, which is shown in Figure 5.8.

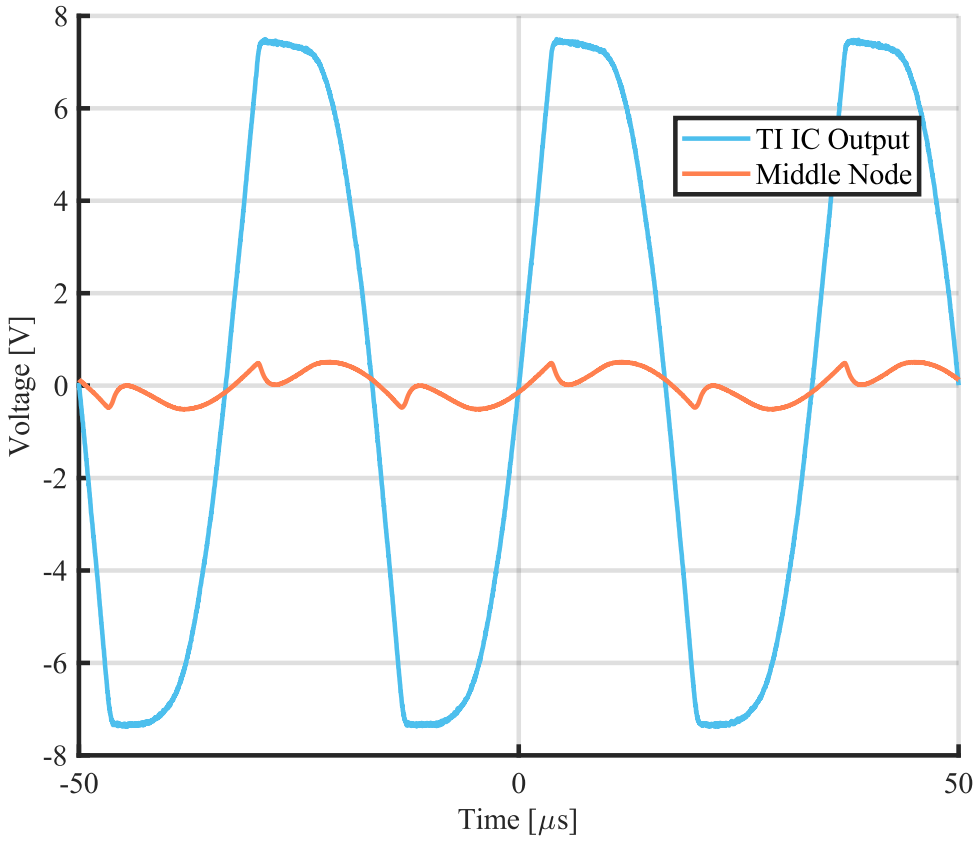

Figure 5.8: TI IC output voltage before its stabilization filter compared to voltage at injection node.

As seen in Figure 5.8, the voltage at the output of the IC is saturated and the voltage is much lower at the injection node, indicating a large voltage drop over the stabilization filter. At low frequencies, the IC is saturated, which leads to reduced noise canceling performance. The weird looking voltage profile at the injection node occurs as a signal similar to a square wave is injected into a circuit consisting of a capacitor, CMC and another capacitor in series, similar to a series-loaded resonant converter.

5.2.3 Different Number of Turns in the CMC

To evaluate the size of the active filter, the OPA690 AEF with 5, 4 and 3 turns in the CMCs was measured and is plotted in Figure 5.9.

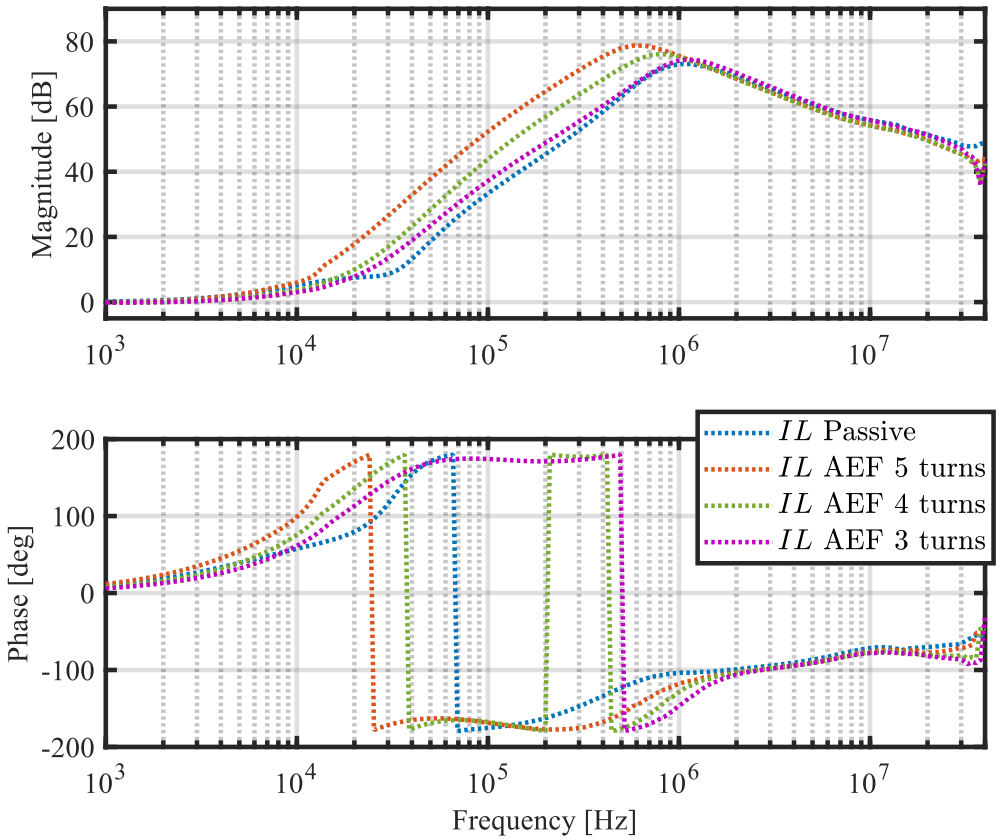

Figure 5.9: Insertion loss of the OPA690 with 5, 4 and 3 turns in the CMCs compared to the passive filter with 5 turns.

The results in Figure 5.9 show, as expected, that a lower number of turns in the CMC gives a lower IL. The AEF with 3 turns has a similar performance to the original passive filter with 5 turns in the CMCs.

An interesting and important note is that after 1 MHz, all filters behave the same. This shows that the insertion loss for high frequencies neither depends on the capacitance nor the inductance in the CMCs.

5.2.4 Low Voltage Performance Summary

The low voltage IL performance measurements prove that all active filters reduce the emitted CM disturbances up to 1 MHz. All Op-amps are performing equally, meaning that voltage swing and current limitations are the most important factors for selecting an Op-amp. The TI IC has a greater attenuation, but its maximum current is very limited due to the much higher output impedance of its Lead-Lag filter. It is also important to note that at higher frequencies, neither inductance nor capacitance seems to affect the attenuation of the filter.

5.3 High Voltage Performance Verification

In this section, high voltage verifications are presented. The DC/DC converter with various combinations of filters was operating at 700 V at 20 kW. A limit curve according to UN ECE R10 Rev.6 maximum conducted emissions on DC power lines is plotted as a reference in the measurements [10]. First, the AEF with OPA690 was compared to the passive filter, followed by a comparison of all Op-amps. Thereafter, the AEF with 4 turns in the CMCs was compared to the passive filter with the same number of turns, followed by the performance of the TI IC.

5.3.1 Active vs Passive Filtering Performance

The measurements from existing passive EMI filter compared to the implemented AEF are presented in Figure 5.10.

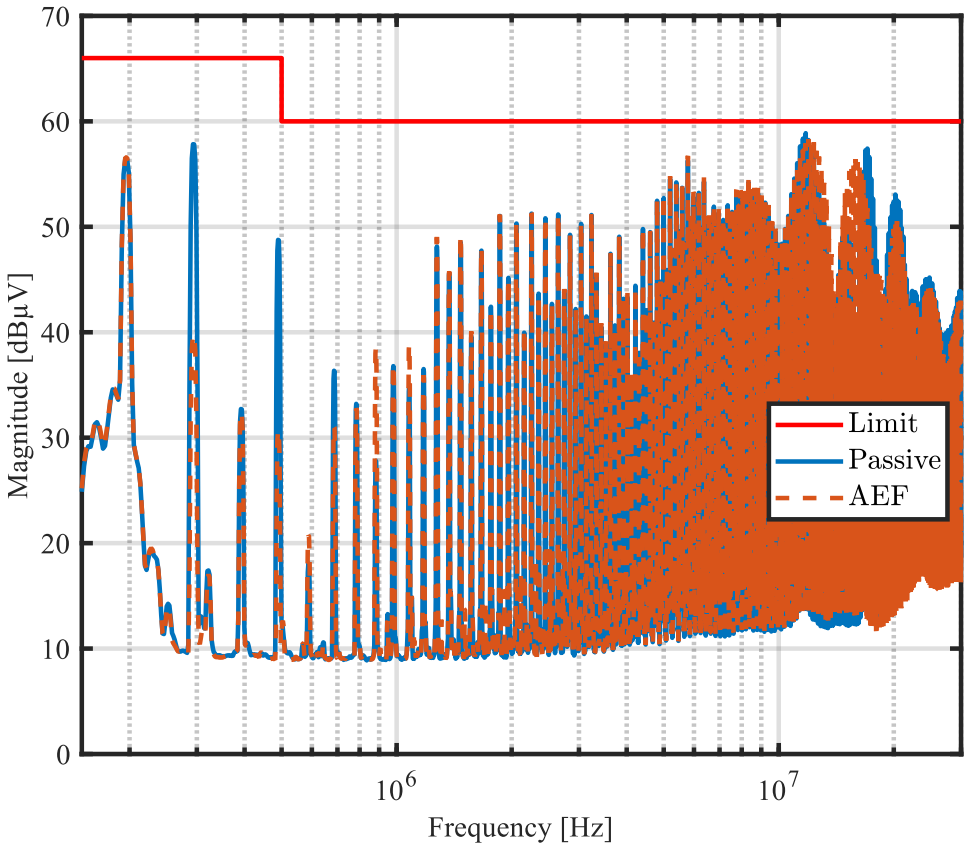

Figure 5.10: Conducted EMI emissions at 20 kW measured at LISN ports.

The measurements in Figure 5.10 contain the conducted disturbances which consist of both CM and DM noise. The peak at 200 kHz is mainly due to DM noise and is therefore not affected by neither the passive CM filter nor the AEF. However, the first CM peaks at 300 kHz, 500 kHz and 700 kHz are reduced by 18.09 dB µV,

17.66 dB µV and 5.32 dB µV respectively.

There is however, a decrease in the disturbance at 900 kHz which is unexpected. It is unclear why, but as it is one specific frequency, it could be a resonance in the passive filter, resulting in a very large attenuation, or some resonance that is decreasing the performance of the active filter. However, the magnitude of the peak is in the same range as the other nearby peaks and will not have any important implications for the overall performance.

The output voltage of the Op-amp measured against ground is given in Figure 5.11

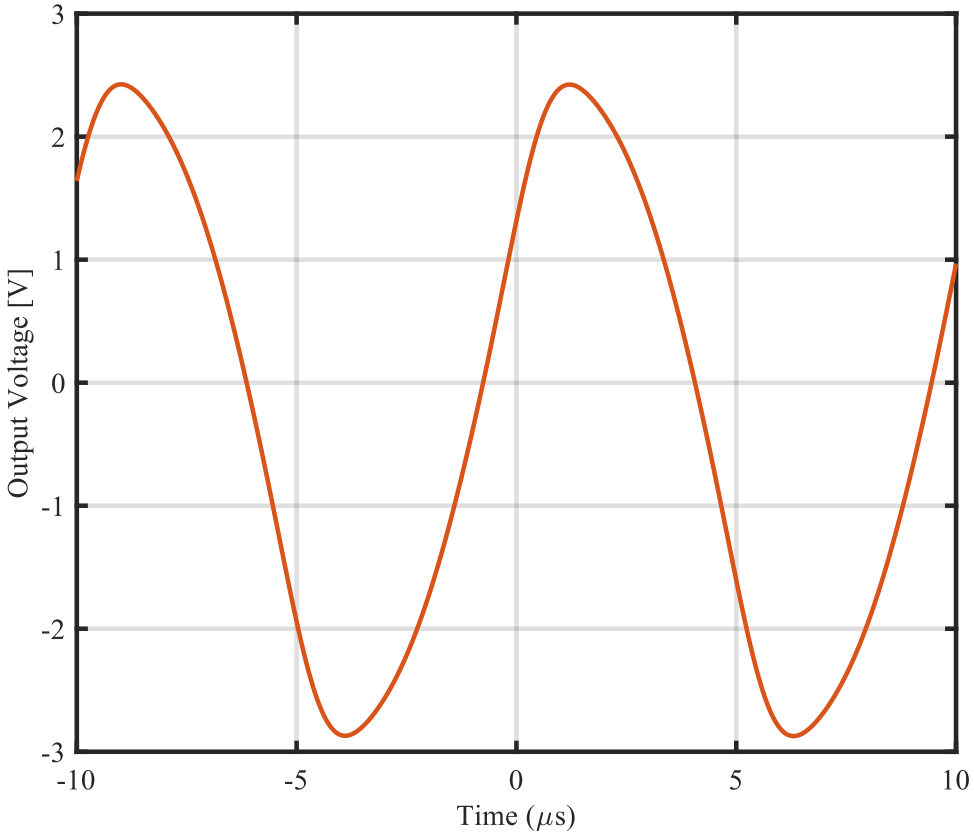

Figure 5.11: OPA690 output voltage.

The voltage in Figure 5.11 is within the voltage swing of the Op-amp. The fundamental frequency of the voltage is the switching frequency of 100 kHz for the EUT. As 100 kHz is outside the measured EMI spectrum (below 150 kHz), this is unnecessary. Possibly, a sharp band-block filter could reduce the output current and voltage substantially without affecting the EMI measurements by blocking the switching frequency from being amplified in the AEF. The output current of the Op-amp was also measured to a peak amplitude of 42 mA which is less than the output current limit of all Op-amps.

The distinction between CM and DM noise can be done by measuring the conducted emissions with a TEKBOX LISN MATE that separates the DM and CM noise. The DM noise is presented in Figure 5.12.

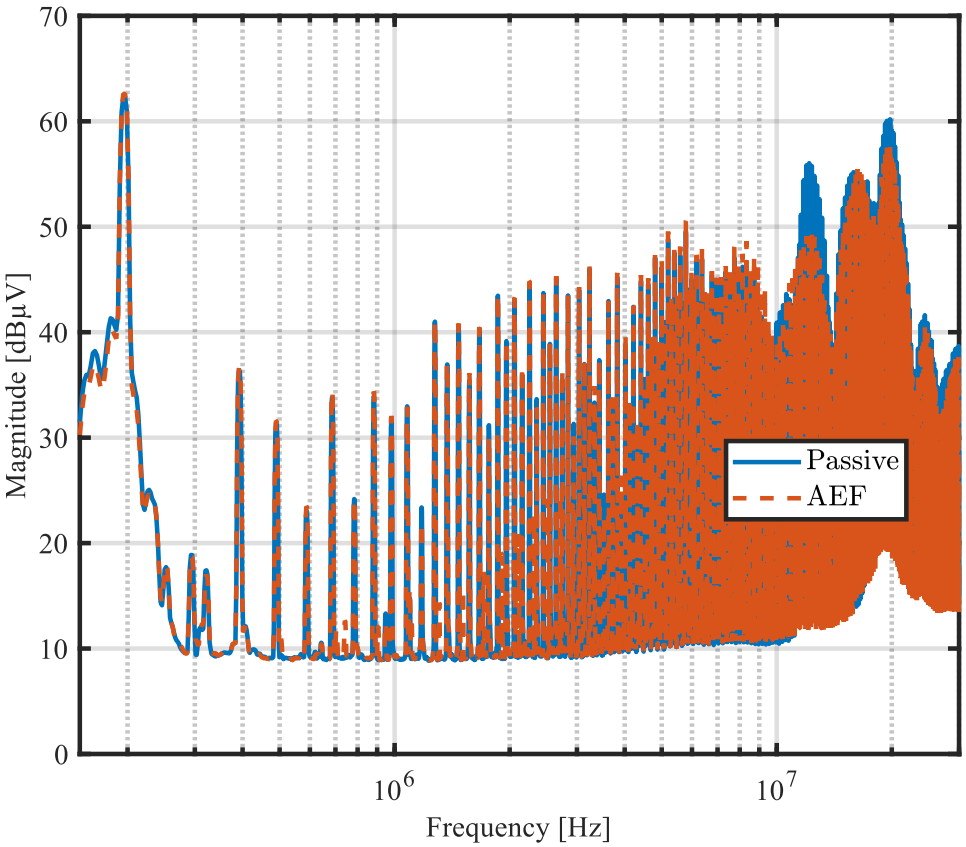

Figure 5.12: Differential mode EMI emissions at 20 kW measured with LISN MATE.

Figure 5.12 proves that the peaks at 200 kHz and 400 kHz are DM and that they are not affected by the AEF, meaning that the AEF does not affect the DM noise.

The CM noise was also measured with the LISN MATE and is presented in Figure 5.13.

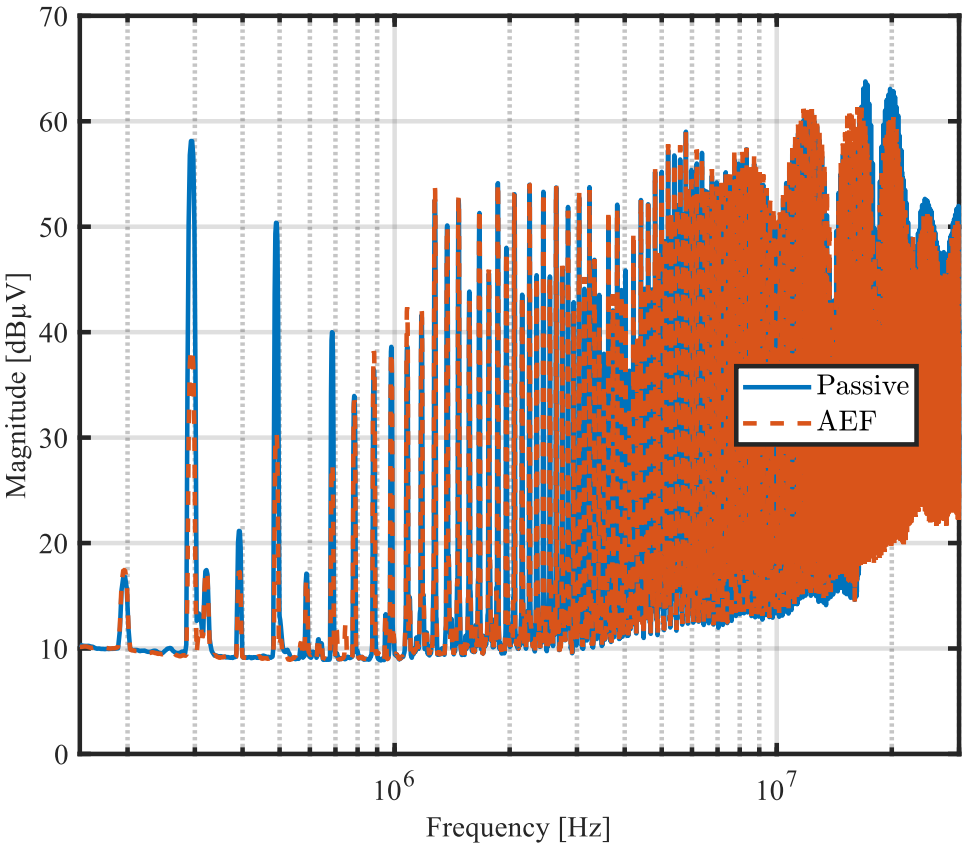

Figure 5.13: CM EMI emissions at 20 kW measured with LISN MATE.

The CM emissions in Figure 5.13 are as previously stated mainly at 300 kHz, 500 kHz and 700 kHz. The AEF is suppressing these noise peaks.

5.3.2 Op-amp Comparison

The emitted EMI noise for all Op-amps is presented in Figure 5.14.

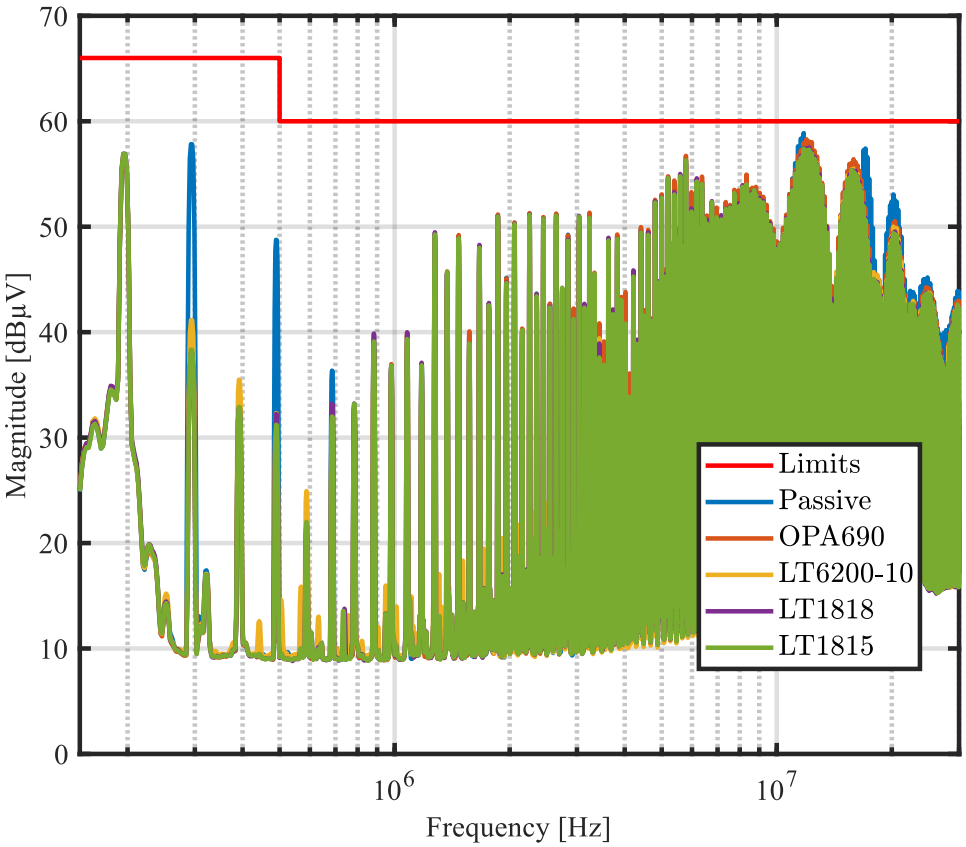

Figure 5.14: EMI emissions for all Op-amps and the passive filter.

All Op-amps perform equally in Figure 5.14, although LT6200-10 is slightly worse than the rest. This is probably due to the lower current limitations. When the output current gets close to the limit, the Op-amp may start to suffer in amplification performance.

Figure 5.15 shows a zoomed in view of Figure 5.14 of the relavant frequency range of the first three CM peaks.

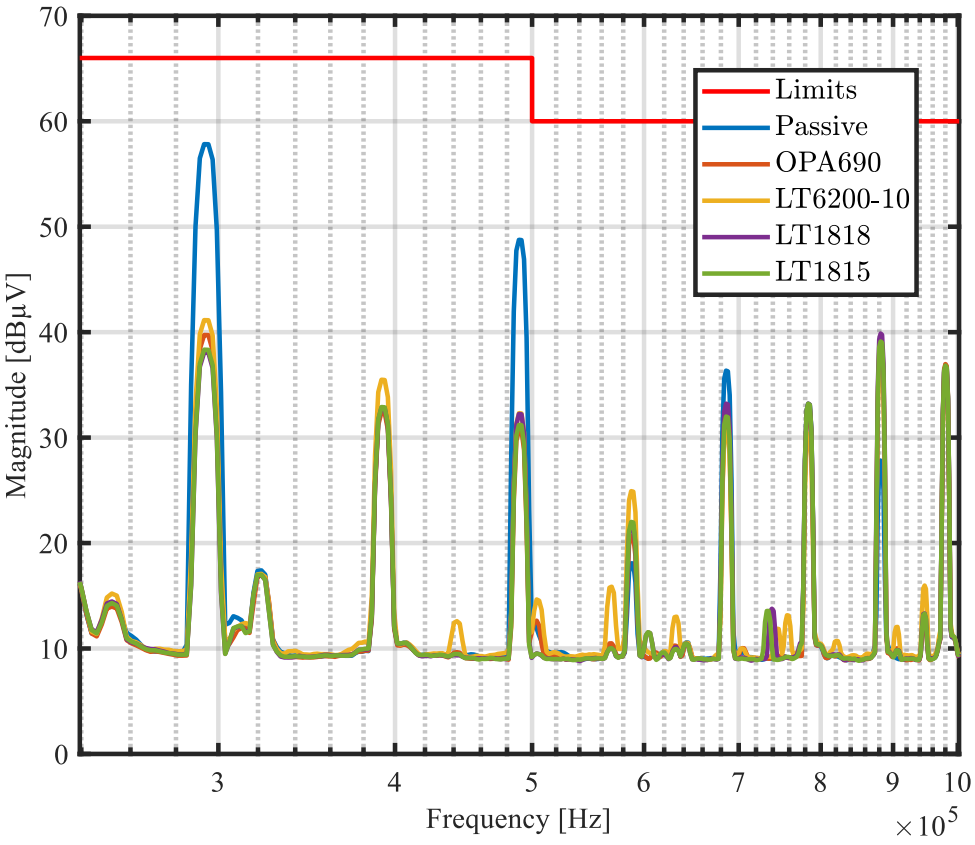

Figure 5.15: A zoomed in view of EMI emissions for all Op-amps and the passive filter.

From Figure 5.15, it becomes more clear that all Op-amps are performing similarly.

5.3.3 Performance with 4 Turns in the CMCs

The EMI noise for filters with the number of turns in the CMC reduced to four is presented in Figure 5.16.

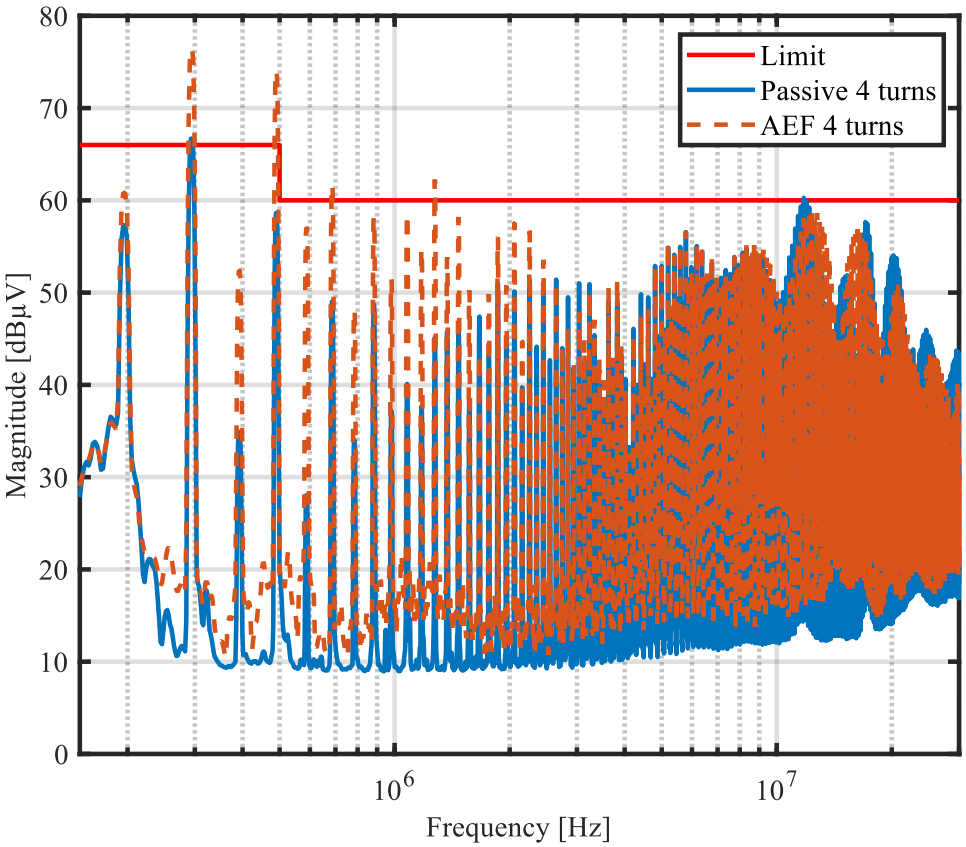

Figure 5.16: EMI emissions at 20 kW measured at LISN with 4 turns CMCs.

In the case of only 4 turns in the CMC, shown in Figure 5.16, the AEF performs worse than the passive filter. To understand why, the output voltage of the Op-amp was measured and is presented in Figure 5.17

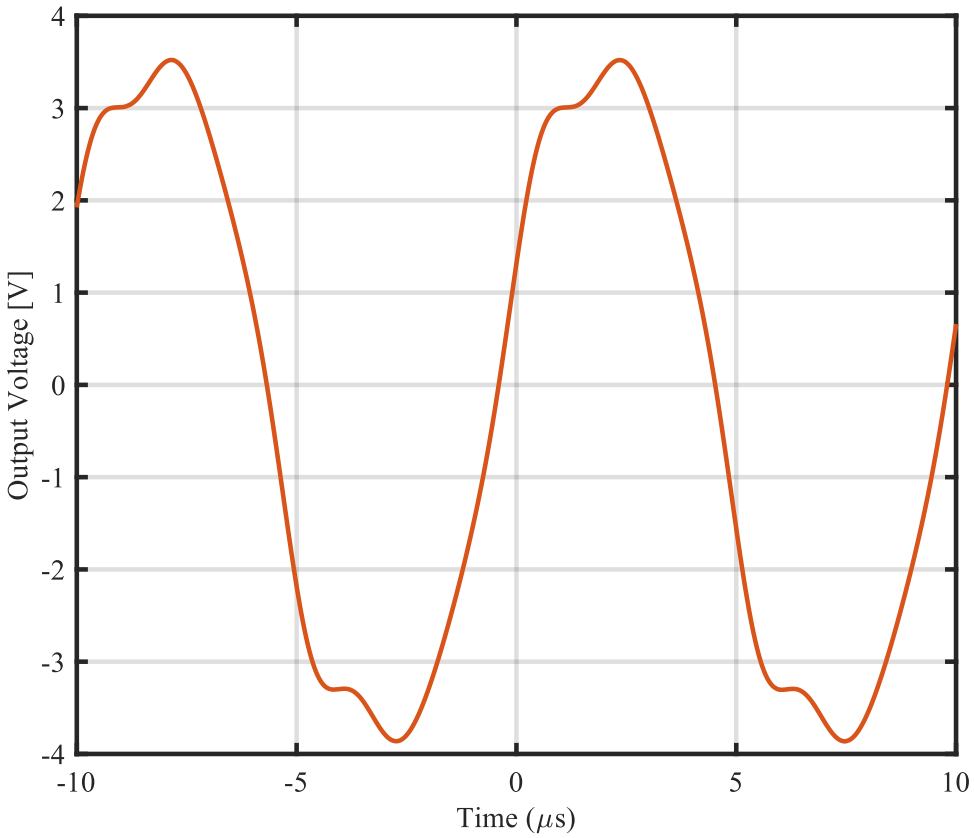

Figure 5.17: OPA690 output voltage and current with 4 turns CMCs.

In Figure 5.17, the output voltage of the Op-amp is distorted and is probably at the output swing of approximately $\pm$ 3.5 V which distorts the signal and induces noise instead of attenuating the noise. The AEF output current was measured to an amplitude of 85 mA which is higher than all Op-amps except OPA690.

An attempt to get a 4 turn CMC AEF to work was done by lowering the Op-amp gain, to hopefully reduce the attenuation in order to lower the output voltage and not drive the Op-amp to its limit. The results of which are presented in Figure 5.18.

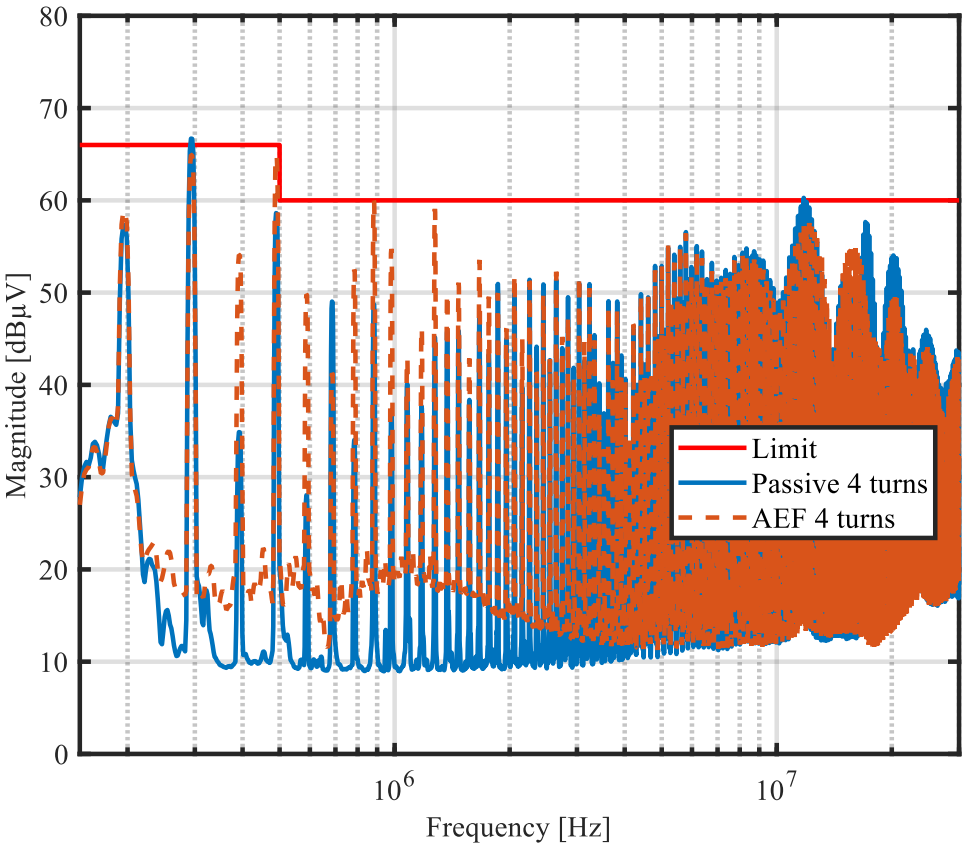

Figure 5.18: EMI emissions at 20 kW measured at LISN with 4 turns CMCs. With lowered AEF gain to 10.

In Figure 5.18, it is seen that the AEF with decreased gain still performs worse than the passive filter for most frequencies.

The output voltage was measured and is presented in Figure 5.19.

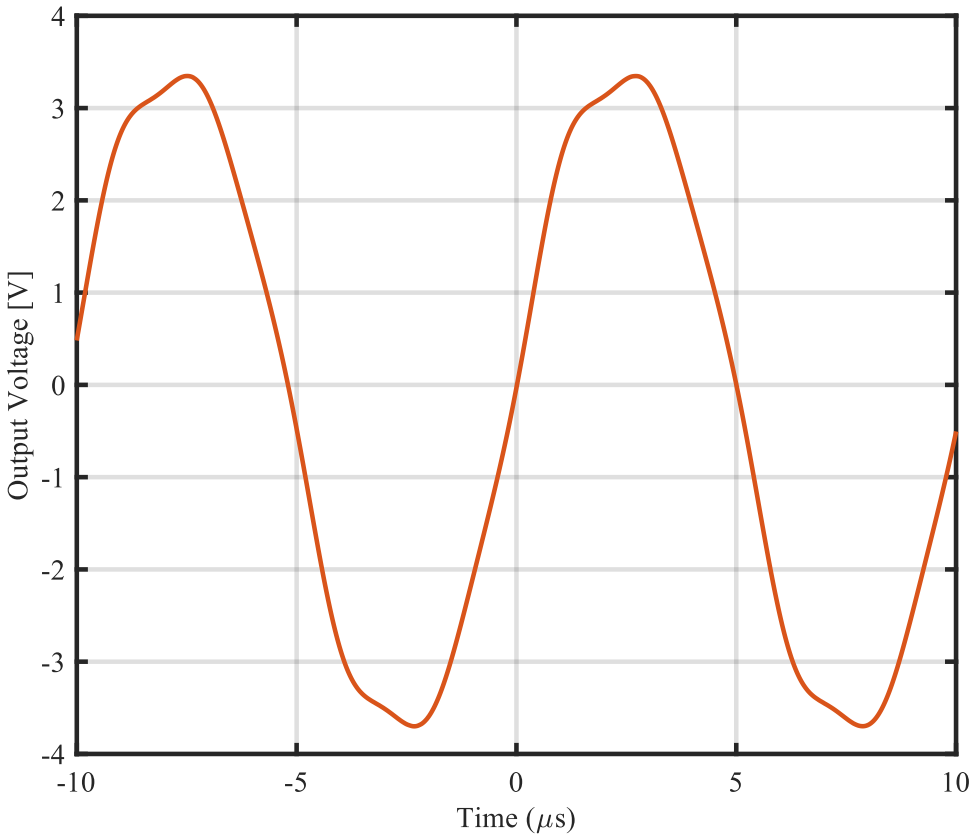

Figure 5.19: OPA690 output voltage with 4 turns CMCs and 10 in Gain.

Figure 5.19 shows that the Op-amp is still operating at its limits and the voltage gets a bit distorted, which explains why it still does not perform better than the passive filter. The output current of the 10 gain AEF with 4 turns CMC was measured to 100 mA, which is still higher than most Op-amps can handle. Note that reducing the gain to 10 did not solve the saturation issue.

5.3.4 Performance of Texas Instruments IC

The EMI spectrum noise for Texas Instruments IC is presented in Figure 5.20.

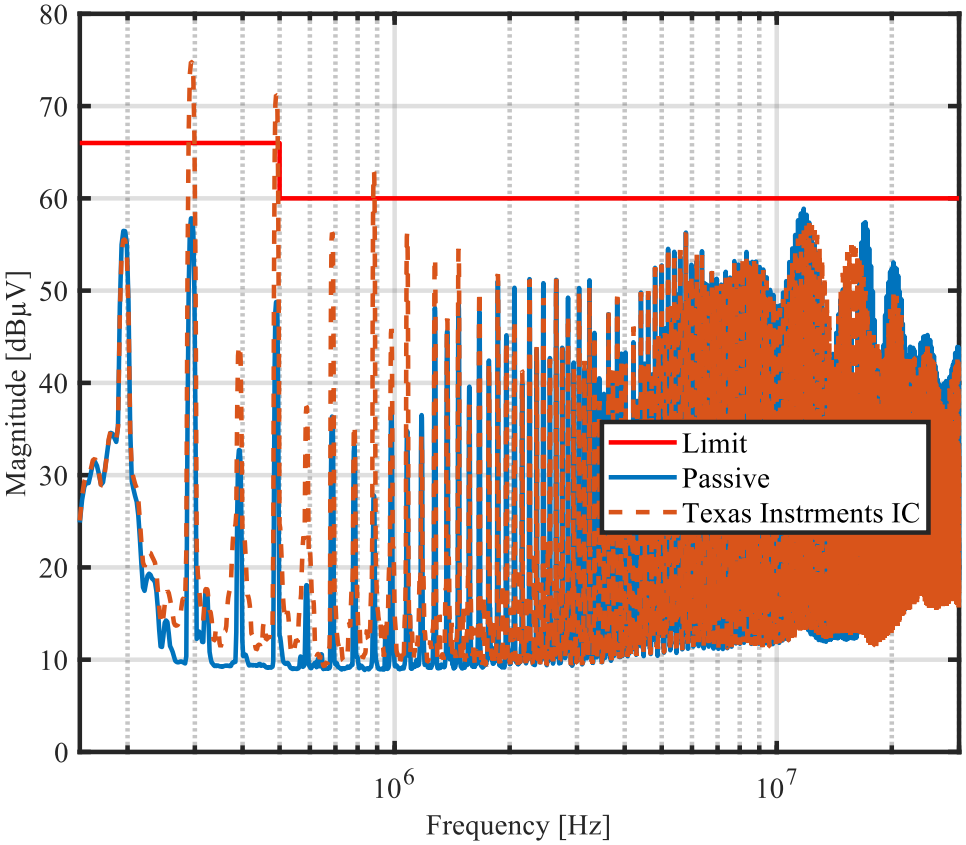

Figure 5.20: EMI emissions at 20 kW for Texas Instruments IC measured at LISN with 5 turns CMCs.

The active filter using Texas Instruments IC performed worse than the passive filter over a large frequency range. Even the emissions with frequencies corresponding to the differential mode noise are increased substantially. That means that the filter emits disturbances instead of canceling them, which most probably is due to a distorted injection current. To further analyze the issue, the output voltage was measured and is given in Figure 5.21.

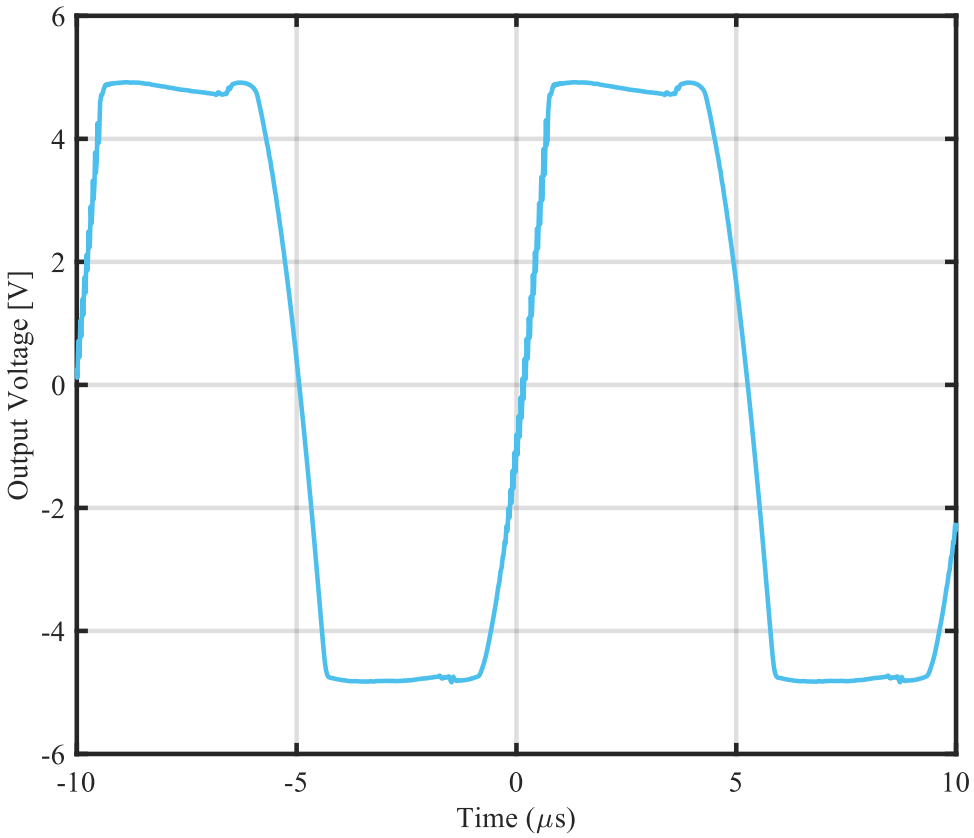

Figure 5.21: Texas EVM Output voltage with 5 turns CMC

Figure 5.21 indicates that the Texas Instruments evaluation board is outputting its maximum voltage and is saturated, possibly causing disturbances in all frequencies, similar to the low voltage case. Because there is a large voltage drop in the output filter, the voltage reaching the injection capacitor is much lower. Similar to the case with the Op-amp, the fundamental frequency is the switching frequency of 100 kHz. A sharp band-block filter could possibly reduce the output voltage and increase its performance.

5.3.5 High Voltage Performance Summary

The high voltage verifications show that similarly to the low voltage IL measurements, the AEF performs well up to about 1 MHz to then have similar performance as the passive filter for the rest of the frequency range. The separation of CM and DM noise with the TEKBOX LISN MATE shows that the AEF does not affect DM noise and only reduces CM noise with a peak performance of 18.09 dB µV reduction for the first CM noise peak.

The fundamental frequency of the output voltage is the switching frequency of the EUT. This frequency is outside the measured conducted noise spectra. A possible implementation of a sharp band-block filter at the switching frequency would sig-

nificantly increase the headroom of the AEF. This may enable a reduction of CMC turns as the AEF would not saturate at the switching frequency.

The performance comparison between Op-amps for the AEF shows no meaningful difference. The gain bandwidth product varies greatly between the Op-amps but shows no significant effects. This is due to the high frequency compensation that is implemented to ensure stability.

The limiting factor for AEF performance for a reduction of CMC turns to 4 is the supplied voltage. The AEF saturates and induces noise instead of reducing noise if the magnitude of the disturbances is too large. The possible reduction to 3 CMC turns with similar performance to the passive filter shown in low voltage verification is not applicable in this case. The higher voltage creates a larger noise amplitude and saturates the AEF. To successfully have 4 or 3 turns CMCs and AEF perform similar to a passive filter with 5 CMC turns, a more powerful amplifier that can supply more voltage is suggested.

5.4 Passive Filter Size and Power Requirements

It has previously been suggested in the Low Voltage Performance Verification that the AEF with 3 turns in the CMCs performed equally to the passive filter with 5 turns. As the inductance is proportional to the square of the number of turns, the inductance can be lowered by approximately 64 %. Furthermore, the inductance is proportional to the reluctance, meaning that the cross-sectional area, the volume and weight of the core can be reduced by 64 %. In addition, the copper of two turns is removed, which corresponds to approximately 40 % of the copper needed in the chokes.

The time domain measurements show that the peak value of the output current of the Op-amp is at max in the range of 100 mA and the peak value of the voltage is approximately 3.5 V. That means that the output power of the AEF is at maximum 0.18 W, which is negligible for a converter operating at 20 kW.

5.5 Ethical and Environmental Considerations

The usage of active EMI filters compared to purely passive filters can have environmental and ethical impacts that should be considered. The following section aims to discuss a few of these topics.

Active filtering will reduce the need for passive components, which will save material needed to produce the product. Especially copper and ferrite savings, which are minerals that are prone to be bad for the environment in their production.

The reduced size and weight of the product can also be an energy saving technique, especially for products placed in transportation equipment. A weight reduction of

such a product will reduce the weight of the whole vehicle, which will reduce its energy consumption during its whole lifetime.

Active filters can be very specialized and tuned to only work in the specified range for the requirements. It can be discussed whether or not this is ethical. Especially in the case of possibly implementing a band block filter to not cancel the switching frequency, which is the strongest disturbance. However, if a solution passes the legal and other requirements, it is deemed that this is an issue with the requirements.

There is also a reliability issue with active filters. A passive filter is much more robust, while an active filter can fail. For example, due to overvoltages at the Op-amp. In that case, the product will most probably function as intended for the user, and this fault may not be noticed, but will lead to a lot more noise being emitted into the grid or other equipment. In such cases, the user will most probably continue to use the product even if it emits noise.

6
Conclusion

This report has investigated the implementation of an active EMI filter to complement an existing passive EMI filter to enhance the mitigation of CM noise in a DC/DC converter. The AEF is shown to perform better than a traditional passive EMI filter in the range of 150 kHz to 700 kHz with an increased noise attenuation of 18 dB µV. It is also shown that the limiting factor at high frequencies is neither the capacitance nor the CMCs, meaning that for this application, an AEF with this topology cannot be used for higher frequencies.

All tested Op-amps have the same performance, since the bandwidth and gain are set by discrete components, provided the Gain Bandwidth Product exceeds the selected gain and bandwidth. In contrast, the voltage and current capabilities are the most important factors in Op-amp selection for AEF.

The increase in attenuation of AEFs indicates that CMCs can be reduced in size while maintaining performance, as shown by the low voltage verification. With a higher amplification capability, the size and weight of the common mode chokes can be reduced by approximately 64 %. It is therefore concluded that the implementation of an active filter can indeed reduce the overall size and footprint of an EMI filter.

The TI off the shelf IC can have high performance and has a higher insertion loss compared to the own developed filter using an Op-amp. However, since the stabilization filter is placed at the output, it introduces a high output impedance that substantially limits the filter's current capacity. For certain applications, the IC can work, but for custom applications, an Op-amp driven AEF is a must.

6.1 Future Work

In order to get the AEF to perform with fewer CMC turns, the voltage supply of the injection cancellation signal must be increased to cope with the higher noise amplitudes resulting from fewer CMC turns. Increasing the voltage on the Op-amps is not feasible, as they can only handle ± 6 V. A larger voltage than this is needed. Therefore, a better amplifier is needed, for example a Push-pull amplifier.

Another critical aspect is how to reduce the noise for higher frequencies. It could be

interesting to investigate the effect of placing the AEF near the output rather than between the CMCs. This would decrease the order of the filter, but could perhaps work at higher frequencies if the signal does not bypass in the same way as for an AEF between the CMCs. It could also be interesting to investigate if two active filters can be used, one between the chokes for low frequencies and one at the output tuned for higher frequencies.

Bibliography

[1] Y. Chu, S. Wang, and Q. Wang, "Modeling and Stability Analysis of Active/Hybrid Common-Mode EMI Filters for DC/DC Power Converters," *IEEE Transactions on Power Electronics*, vol. 31, no. 9, pp. 6254–6263, Sep. 2016, ISSN: 08858993. DOI: 10.1109/TPEL.2015.2502218. [Online]. Available: https://ieeexplore.ieee.org/document/7332787.

[2] K. Mainali and R. Oruganti, "Conducted EMI mitigation techniques for switch-mode power converters: A survey," *IEEE Transactions on Power Electronics*, vol. 25, no. 9, pp. 2344–2356, 2010, ISSN: 08858993. DOI: 10.1109/TPEL.2010.2047734. [Online]. Available: https://ieeexplore.ieee.org/document/5444974.

[3] W. Chen, X. Yang, and Z. Wang, "An active EMI filtering technique for improving passive filter low-frequency performance," *IEEE Transactions on Electromagnetic Compatibility*, vol. 48, no. 1, pp. 172–177, Feb. 2006, ISSN: 00189375. DOI: 10.1109/TEMC.2006.870803. [Online]. Available: https://ieeexplore.ieee.org/document/1614050.

[4] W. Chen, W. Zhang, X. Yang, Z. Sheng, and Z. Wang, "An experimental study of common- and differential-mode active EMI filter compensation characteristics," *IEEE Transactions on Electromagnetic Compatibility*, vol. 51, no. 3, pp. 683–691, Aug. 2009, ISSN: 00189375. DOI: 10.1109/TEMC.2009.2021258. [Online]. Available: https://ieeexplore.ieee.org/document/5062294.

[5] T. Hegarty, "How Active EMI Filter ICs Mitigate Common-Mode Emissions and Increase Power Density in Single- and Three-Phase Power Systems," Texas Instruments, Dallas, Tech. Rep., Mar. 2023. [Online]. Available: https://www.ti.com/lit/wp/slvafj9/slvafj9.pdf?ts=1771497723011.

[6] F. Costa, C. Gautier, E. Labouré, and B. Revol, *Electromagnetic Compatibility in Power Electronics*, B. Multon, Ed. Hoboken: ISTE ; Wiley, 2014, pp. 214–221, ISBN: 9781848215047.

[7] Q. Chen, R. Zhang, Z. Niu, and C. Gong, "Frequency Characteristics of Insertion Loss and Loop Gain of VSCC Feedback Active EMI Filters," *IEEE Transactions on Electromagnetic Compatibility*, vol. 67, no. 1, pp. 139–148, Feb. 2025, ISSN: 1558187X. DOI: 10.1109/TEMC.2024.3454127. [Online]. Available: https://ieeexplore.ieee.org/document/10693308.

[8] B. Narayanasamy and F. Luo, "A Survey of Active EMI Filters for Conducted EMI Noise Reduction in Power Electronic Converters," *IEEE Transactions on Electromagnetic Compatibility*, vol. 61, no. 6, pp. 2040–2049, Dec. 2019, ISSN: 1558187X. DOI: 10.1109/TEMC.2019.2953055. [Online]. Available: https://ieeexplore.ieee.org/document/8915991.

[9] Texas Instruments, "TPSF12C1 Standalone, Active, EMI Filter for Common-mode Noise Mitigation in Single-Phase, AC, Power Systems TPSF12C1 Simplified Schematic EMI Mitigation Result TPSF12C1," Texas Instruments Incorporated, Tech. Rep., Apr. 2023. [Online]. Available: https://www.ti.com/lit/ds/symlink/tpsf12c1.pdf?ts=1776272771865&ref_url=https%253A%252F%252Fhu.mouser.com%252F.

[10] *Agreement Concerning the Adoption of Harmonized Technical United Nations Regulations for Wheeled Vehicles, Equipment and Parts which can be Fitted and/or be Used on Wheeled Vehicles and the Conditions for Reciprocal Recognition of Approvals Granted on the Basis of these United Nations Regulations**, Nov. 2019. [Online]. Available: https://unece.org/fileadmin/DAM/trans/main/wp29/wp29regs/2019/E-ECE-324-Add.9-Rev.6.pdf.

[11] F. Costa, C. Gautier, E. Labouré, and B. Revol, *Electromagnetic Compatibility in Power Electronics*, B. Multon, Ed. Hoboken: ISTE ; Wiley, 2014, pp. 30–41, ISBN: 9781848215047.

[12] Murata, *Differential and CommonMode Noise*. [Online]. Available: https://www.murata.com/~/media/webrenewal/products/emc/emifil/knowhow/26to30.ashx.

[13] Coilcraft, *A Guide to Understanding Common Mode Chokes*. [Online]. Available: https://www.coilcraft.com/en-us/edu/series/a-guide-to-understanding-common-mode-chokes/.

[14] J. L. Kotny, T. Duquesne, and N. Idir, "Design of EMI filters for DC-DC converter," in *2010 IEEE Vehicle Power and Propulsion Conference, VPPC 2010*, IEEE Computer Society, 2010, ISBN: 9781424482191. DOI: 10.1109/VPPC.2010.5729047. [Online]. Available: https://ieeexplore.ieee.org/document/5729047.

[15] Z. Zhu, Y. Zhao, W. Yan, X. Liu, and M. Ju, "Modeling of line impedance stabilization network impedance characteristic based on genetic algorithm," *Microelectronics Journal*, vol. 113, p. 105 095, 2021, ISSN: 1879-2391. DOI: https://doi.org/10.1016/j.mejo.2021.105095. [Online]. Available: https://www.sciencedirect.com/science/article/pii/S0026269221001063.

[16] M. Eaker and D. Berger, "Understanding CISPR25 Current Probe and Voltage Method for Conducted Emissions," Dallas, Apr. 2025. [Online]. Available: https://www.ti.com/lit/ab/slla569b/slla569b.pdf?ts=1772391361355.

[17] IEC, *INTERNATIONAL STANDARD CISPR 25*, Geneva, Oct. 2016.

[18] "HV-AN 150 datasheet_e06," Teseq, Tech. Rep., Aug. 2021. [Online]. Available: https://www.ametek-cts.com/-/media/ametekcts/importdata/documents/datasheets/teseq/hv_an_150_datasheet_e06.pdf?la=en&revision=149328e5-81b8-4da1-809e-f283e1504478.

[19] R. Goswami and S. Wang, "Modeling and Stability Analysis of Active Differential-Mode EMI Filters for AC/DC Power Converters," *IEEE Transactions on Power Electronics*, vol. 33, no. 12, pp. 10 277–10 291, Dec. 2018, ISSN: 08858993. DOI: 10.1109/TPEL.2018.2806361. [Online]. Available: https://ieeexplore.ieee.org/document/8292878.

[20] *S-Parameter Insertion Loss in the Development of Microwave Circuits | System Analysis Blog | Cadence*. [Online]. Available: https://resources.system-analysis.cadence.com/blog/msa2021-the-importance-of-s-parameter-insertion-loss-in-the-design-and-development-of-microwave-circuits.

[21] L. LaWhite and M. F. Schlecht, "Design Of Active Ripple Filters For Power Circuits Operating In The 1-10 Mhz Range," *IEEE Transactions on Power Electronics*, vol. 3, no. 3, pp. 310–317, Jul. 1988, ISSN: 19410107. DOI: 10.1109/63.17949. [Online]. Available: https://ieeexplore.ieee.org/document/17949.

[22] N. K. Poon, J. C. Liu, C. K. Tse, and M. H. Pong, "Techniques for input ripple current cancellation: classification and implementation," *IEEE Transactions on Power Electronics*, vol. 15, no. 6, pp. 1144–1152, Nov. 2000, ISSN: 08858993. DOI: 10.1109/63.892829. [Online]. Available: https://ieeexplore.ieee.org/document/892829.

[23] Y. C. Son and S. K. Sul, "Generalization of active filters for EMI reduction and harmonics compensation," *IEEE Transactions on Industry Applications*, vol. 42, no. 2, pp. 545–551, Apr. 2006, ISSN: 00939994. DOI: 10.1109/TIA.2006.870030. [Online]. Available: https://ieeexplore.ieee.org/document/1608233.

[24] S. Jeong, D. Shin, and J. Kim, "A Transformer-Isolated Common-Mode Active EMI Filter Without Additional Components on Power Lines," *IEEE Transactions on Power Electronics*, vol. 34, no. 3, pp. 2244–2257, Mar. 2019, ISSN: 08858993. DOI: 10.1109/TPEL.2018.2845467.

[25] K. Mainali and R. Oruganti, "Design of a current-sense voltage-feedback common mode EMI filter for an off-line power converter," *PESC Record - IEEE Annual Power Electronics Specialists Conference*, pp. 1632–1638, 2008, ISSN: 02759306. DOI: 10.1109/PESC.2008.4592174.

[26] D. Shin, S. Jeong, and J. Kim, "Quantified Design Guidelines of a Compact Transformerless Active EMI Filter for Performance, Stability, and High Voltage Immunity," *IEEE Transactions on Power Electronics*, vol. 33, no. 8, pp. 6723–6737, Aug. 2018, ISSN: 08858993. DOI: 10.1109/TPEL.2017.2763972. [Online]. Available: https://ieeexplore.ieee.org/document/8069035.

[27] C. E. Kurien, T. K. Sindhu, and D. E. Koshy, "Modelling and Implementation of an Active EMI Filter for Conducted EMI Noise Reduction," in *Proceedings of 2021 5th International Conference on Condition Assessment Techniques in Electrical Systems, CATCON 2021*, Institute of Electrical and Electronics Engineers Inc., 2021, pp. 205–210, ISBN: 9780738112916. DOI: 10.1109/CATCON52335.2021.9670535. [Online]. Available: https://ieeexplore.ieee.org/document/9670535.

[28] J. Aigner, M. Lemke, M. Ambaum, T. Dorlemann, and S. Frei, "Digital Active CM EMI Suppression of a DC-DC Converter with Synthesized Switching-Slope Dependent Cancellation Pulses," *Proceedings of the International Symposium on Electromagnetic Compatibility, EMC Europe*, no. 2025, pp. 813–818, 2025, ISSN: 23250364. DOI: 10.1109/EMCEUROPE61644.2025.11176360. [Online]. Available: https://ieeexplore.ieee.org/document/11176360.

[29] S. Jeong, D. Shin, J. Kim, J. Kim, and S. Kim, "Design of effective surge protection circuits for an active EMI filter," in *2017 Asia-Pacific International Symposium on Electromagnetic Compatibility, APEMC 2017*, Institute of Electrical and Electronics Engineers Inc., Jul. 2017, pp. 210–212, ISBN: 9781538639122. DOI: 10.1109/APEMC.2017.7975464. [Online]. Available: https://ieeexplore.ieee.org/document/7975464.

[30] B. Narayanasamy, F. Luo, and Y. Chu, "Modeling and Stability Analysis of Voltage Sensing based Differential Mode Active EMI Filters for AC-DC Power Converters," Long Beach: Institute of Electrical and Electronics Engineers Inc., Oct. 2018, ISBN: 9781538666210. DOI: 10.1109/EMCSI.2018.8495239. [Online]. Available: https://ieeexplore.ieee.org/document/8495239.

[31] S. Cen, "DC Bias Characteristics of Ceramic Capacitors," KYOCERA AVX Components Corporation, Fountain Inn, Tech. Rep. [Online]. Available: https://www.kyocera-avx.com/docs/techinfo/CeramicCapacitors/mlcc-dc-bias-characteristics.pdf.

[32] "EVM User's Guide: TPSF12C1QEVM Active EMI Filter Evaluation Module for Single-Phase AC Power Systems," Texas Instruments, Tech. Rep., Jul. 2023. [Online]. Available: https://www.ti.com/lit/ug/slvuck7a/slvuck7a.pdf?ts=1775554945820&ref_url=https%253A%252F%252Fwww.ti.com%252Fsitesearch%252Fen-us%252Fdocs%252Funiversalsearch.tsp%253FlangPref%253Den-US%2526searchTerm%253DTPSF12C1QEVM%2526nr%253D18.

[33] *TPSF12CX-DESIGN-CALC*. [Online]. Available: https://www.ti.com/tool/TPSF12CX-DESIGN-CALC.

[34] *LTspice*, Analog Devices, Inc. Accessed: Jan. 27, 2026. [Online]. Available: https://www.analog.com/en/resources/design-tools-and-calculators/ltspice-simulator.html.

[35] L. W. Nagel and D. Pederson, "Spice (simulation program with integrated circuit emphasis)," Tech. Rep. UCB/ERL M382, Apr. 1973. [Online]. Available: http://www2.eecs.berkeley.edu/Pubs/TechRpts/1973/22871.html.

[36] *Bode 100, Bode 500 Vector Network Analyzer User Manual*, 2025. [Online]. Available: https://www.omicron-lab.com/fileadmin/assets/Bode-Analyzer-Suite/Documents/Bode-Analyzer-User-Manual.pdf.

[37] OMICRON Lab, *Bode Analyzer Suite*. [Online]. Available: https://www.omicron-lab.com/products/vector-network-analysis/bode-analyzer-suite/.

[38] Mayerhofer, "TBLM1 LISN Mate Manual V 1.3," Tekbox, Tech. Rep., Aug. 2020. [Online]. Available: https://www.tekbox.com/product/TBLM1_LISN_Mate_Manual.pdf.

[39] "OPA690 Wideband, Voltage-Feedback Operational Amplifier With Disable," Texas Instruments, Tech. Rep., Oct. 2024. [Online]. Available: https://www.ti.com/lit/ds/symlink/opa690.pdf?ts=1777417193401&ref_url=https%253A%252F%252Fwww.mouser.com%252F.

[40] B. Lennartson, *Reglerteknikens grunder*, 4. uppl. Lund: Studentlitteratur, 2002, ISBN: 9144024169.

[41] "LT1818/LT1819," Linear Technology, Tech. Rep., 2002. [Online]. Available: https://www.analog.com/media/en/technical-documentation/data-sheets/18189fb.pdf.

[42] "LT1815/LT1816/LT1817," Linear Technology, Tech. Rep., 2001. [Online]. Available: https://www.analog.com/media/en/technical-documentation/data-sheets/181567fb.pdf.

[43] "LT6200_LT6200-5_LT6200-10_ LT6200," Linear Technology, Tech. Rep., 2002. [Online]. Available: https://www.analog.com/media/en/technical-documentation/data-sheets/62001ff.pdf.

[44] Florian Hämmerle, Benjamin Mösslang, "RFI Power Inlet Filter Insertion Loss Measurement," OMICRON Lab, Tech. Rep., 2016. [Online]. Available: https://www.omicron-lab.com/fileadmin/assets/Bode_100/ApplicationNotes/RFI_and_EMC_Filter/App_Note_RFI_Inlet_FIlter_V2.1.pdf.

[45] A. Ruhiyat, F. Kurniawan, and C. Apriono, "Study on Variable Tee and Bridge Tee Attenuators to Enhance IQ Mixer Sideband Suppression in Synthetic Aperture Radar Applications," Singapore: Institute of Electrical and Electronics Engineers Inc., Dec. 2024, ISBN: 9798350350821. DOI: 10.1109/TENCON61640.2024.10902680. [Online]. Available: https://ieeexplore.ieee.org/document/10902680.

DEPARTMENT OF ELECTRICAL ENGINEERING
CHALMERS UNIVERSITY OF TECHNOLOGY
Gothenburg, Sweden 2026
www.chalmers.se

CHALMERS
UNIVERSITY OF TECHNOLOGY